2014

TURBULENT TRANSITION IN ELECTROMAGNETICALLY LEVITATED LIQUID METAL DROPLETS

Jie ZHAO
jzhao@ecs.umass.edu

TURBULENT TRANSITION IN ELECTROMAGNETICALLY LEVITATED LIQUID METAL DROPLETS

A Thesis Presented

by

JIE ZHAO

Submitted to the Graduate School of the

University of Massachusetts Amherst in partial fulfillment

Of the requirements for the degree of

MASTER OF SCIENCE IN MECHANICAL ENGINEERING

May 2014

Mechanical and Industrial Engineering

TURBULENT TRANSITION IN ELECTROMAGNETICALLY LEVITATED LIQUID METAL DROPLETS

A Thesis Presented

by

JIE ZHAO

Approved as to style and content by:

_____

Robert W. Hyers, Chair

_____

Douglas M. Matson, Member

_____

Jonghyun Lee, Member

_____

Donald L. Fisher, Department Head

Mechanical & Industrial Engineering

ACKNOWLEDGMENTS

Thanks to my family.

Thanks to Professor Robert Hyers, Professor Douglas Matson and Professor Jonghyun Lee.

This project has been funded by NASA under grant NNX10AR71G.

ABSTRACT

TURBULENT TRANSITION IN ELECTROMAGNETICALLY LEVITATED LIQUID METAL DROPLETS

May 2014

JIE ZHAO

B.A., UNIVERSITY OF SCIENCE AND TECHNOLOGY, BEIJING

M.S.M.E., UNIVERSITY OF MASSACHUSETTS AMHERST

Directed by: Professor Robert W. Hyers

The condition of fluid flow has been proven to have a significant influence on a wide variety of material processes. In electromagnetic levitation (EML) experiments, the internal flow is driven primarily by electromagnetic forces. In 1-g, the positioning forces are very strong and the internal flows are turbulent. To reduce the flows driven by the levitation field, experiments may be performed in reduced gravity and parabolic flights experiments have been adopted as the support in advance. Tracer particles on the surface of levitated droplets in EML experiment performed by SUPOS have been used to investigate the transition from laminar to turbulent flow. A sample of NiAl3 was electromagnetically levitated in parabolic flight and the laminar-turbulent transition observed from the case was studied in this work. For the sample with clearly visible tracer patterns, the fluid flow has been numerical evaluated with magnetohydrodynamic models and the laminar-turbulent transition happened during the acceleration of the flow, instead of steady state. The Reynolds number at transition was estimated approximately as 860 by the experiment record. The predicted time to transition obtained from the results of simulation showed significant difference (~ up to 300 times) compared with the time obtained from the experiment—0.37s.

The discrepancy between numerical and experimental results could not be explained by the proposed hypotheses: geometry, boundary conditions or solid core. The simulations predict that

the flow would become turbulent almost instantaneously after the droplet was fully molten. There are important physics shown by the simulation which were not captured.

TABLE OF CONTENTS

Page

NOMENCLATURE

u: Velocity field

t: Time

P: Pressure

Re: Reynolds number

F: Force

B: Magnetic field density

FL: Lorentz force

I: Current

Pi: Induced power

ρ: Density

τ_{zx}: Shear stress

$\frac{dv_x}{dz}$: Velocity gradient

Γ: Damping constant

R_0 (r_0): Radius

m: Mass

τ: Damping time

$P_\omega(t)$: Heat power input;

c_P: Specific Heat;

ε: Hemispherical emissivity;

P_0: Constant power on equilibrium temperature;

σ_{SB}: Stefan-Boltzmann constant;

ΔT_ω: Temperature response

$c_{P:}$ Heat capacity

ω: Frequency

J: Eddy current

E: Electrical field

H: Magnetic field

p: Fluid flow pressure;

T: The component of the total stress tensor;

D (d): Diameter;

V: Maximum velocity of inner flow m/s;

μ Viscosity Pa*s;

τ_p is the relaxation time of the particle.

$\sigma(T)$: Electrical conductivity dependent of time, $\Omega^{-1}m^{-1}$;

$\eta(T)$: Viscosity dependent of time, mPa*s;

ρ_m: Density on the melting point;

k: Temperature dependence of density;

T_m: Temperature on the melting point;

LIST OF TABLES

Table Page

LIST OF FIGURES

Figure Page

CHAPTER 1

INTRODUCTION AND BACKGROUND

1.1 Introduction

The convection of molten metals significantly impacts material processing. The fluid flow of molten metals affects the solidification process so that different microstructures result depending on the convection state in the molten metals. In order to obtain desired microstructures, the convection velocity in molten metals should be understood and controlled during solidification. The study of velocity in solidification can be achieved by one of three models: steady-state laminar, steady-state turbulent, and the transient model. The process of turbulence from the laminar flow is called the laminar to turbulent transition. In this work, the turbulent transition in a droplet of $NiAl_3$ was numerically evaluated and certain models have been made.

In addition to solidification, the convection in measurements of thermophysical properties is also crucial. For example, in containerless measurements of viscosity and heat capacity of molten metals, the results are often critically affected by the internal convection. To obtain valid results, the convection when measuring viscosity should be laminar. Measurements of heat capacity, however, benefit from an internal turbulence flow. This study of the turbulent transition clarifies the upper limit of laminar and lower one of turbulence. The results of this study will improve the design of measurements for thermophysical properties which are essential for solving Navier-Stokes equations.

This work also improves the study of turbulence. By changing the method of observation, the turbulent transition can be pinpointed more clearly and the corresponding thermophysical state for the numerical modelling can be calculated more accurately. The convection in the liquid

sample is governed by the Navier-Stokes equations, which are characterized by the Reynolds number, a dimensionless ratio of inertial effects to viscous effects. The convection velocity as well as the pressure distribution can be obtained by solving the Navier-Stokes equations. In order to secure the reasonable accuracy of the solution, accurate values for density and viscosity are needed.

The containerless methods of electromagnetic levitation (EML) and electrostatic levitation (ESL) have been adopted to study solidification and thermophysical property measurements. The samples can be levitated without contacting any substance (e.g. the walls of a container) so that a considerable reduction of contamination can be achieved and many highly-reactive materials can be tested. Moreover, the effect of walls on nucleation can be eliminated.

Previous work showed that only high-velocity turbulent flow could be obtained from ground-based EML. Strong convection observed in samples is induced by the strong positioning force required to counteract gravity. Meanwhile, in ground-based ESL, only low-velocity laminar flow caused by gradients in surface tension is found. This is called Marangoni convection. There is an obvious gap between the two ranges, which means the full range of convection is not accessible in ground-based experimentation.

Space provides an environment without the disturbance of gravity to study solidification and measure material properties. In space, the convection in the sample is not as strong as on Earth because the force necessary to counteract gravity is not required. Thus, the electromagnetic levitation technique has been adopted as a processing method in space due to its advantages over other containerless processing techniques.

Thus, a much wider range of convection from the laminar to turbulent flow can be achieved by space EML. It is very expensive to achieve EML experiments in space. The experiment needs to be predicted to ensure it runs well. Parabolic flight experiments are an important part of ground

support for space experiments. For example, in order to guarantee the safety of astronauts and facilities, the space samples have to be tested in parabolic flights ahead of time. For example, if the sample became unstable or even escaped from the holders during the parabolic flight experiment, it would be too dangerous to test it in space. It may damage any substances making contact with it and ruin the whole experiment. The tests should be redesigned. To ensure the space experiments' safety, the parabolic flights data should be analyzed. Due to the complexity level of the system, the numerical analysis of the parabolic flights data is essential as ground support to experimentation in space.

Understanding this transition phenomenon observed in parabolic flight is important in that it allows more efficient design of space experiments. A large uncertainty in the range of Re during transition enforces the use of a large safety factor in determining the measurable range of experimental parameter settings. A number of compositions will be tested in space from December 2014.

In this work, a parabolic flight experiment with clear evidence of laminar-turbulent transition was selected. In parabolic flights, the electromagnetic force required to control the sample is stronger than in space experiments, leading to severe deformation of sample. In Hyers' work, the Reynolds number at laminar-turbulent transition has been estimated as 600 for a spherical sample. In this work, a new geometry has been adopted: ellipsoid, instead of a sphere. In addition to steady-state models, a new transient model has been developed.

1.2 Motivation

To control the microstructure of the materials, this work developed MHD models to study the convection in molten metals. The measurement of thermophysical properties would be benefited by this study of the effect of the fluid flow in experiments. In addition, the numerical models and simulation result of this laminar-turbulent transition can be adopted by other cases about turbulent

transition. To figure out what possible things can affect the internal convection, three hypotheses needed to be tested: geometry, boundary conditions and solid core.

1.3 Navier-Stokes Equations Application

The convection in molten metals is governed by Navier-Stokes equations, just like other viscous fluid motion.

The N-S equations, named after Claude-Louis Navier and George Gabriel Stokes, are a statement of the conservation of momentum. The equations, derived from the application of conservation of momentum for an arbitrary portion of fluid, have been adopted in various areas to model the flow of liquid. For example, they can be used to describe how fluid flows in the ocean, so that the weather can be forecasted. Furthermore, the N-S Eqns. can be used to model magnetohydrodynamics with Maxwell's equations. Actually, the Navier-Stokes equations can be applied to any non-relativistic continuum.

Navier-Stokes equations—General

$$\nabla^* \cdot u^* = 0 \tag{1.1}$$

$$\frac{\partial u^*}{\partial t^*} + u^* \cdot \nabla^* u^* = -\nabla^* P^* + \frac{1}{Re}\nabla^{*2} u^* + F^* \tag{1.2}$$

where u is velocity field; t is time; P is pressure; F is forces; Re is Reynolds number.

The nonlinear quantity $u^* \cdot \nabla^* u^*$ is the convective acceleration, which is independent of time and coordinate system. The terms ∇p and $\frac{1}{Re}\nabla^{*2} u^*$, which are gradients of surface forces, give the effect of stress in the fluid.

The Navier-Stokes equations can produce a velocity field, providing the velocity of the fluid at a given point in space and time. Other quantities such as flow rate can be found with the velocity field. The velocity field plays a more important role than particle positions or trajectories in classical mechanics.

To apply the Navier-Stokes equations, the internal fluid of the sample is assumed to flow as a continuum, which means it cannot be divided into particles like atoms or molecules. The Navier-Stokes equations was used to model the internal fluid flow with fixed boundary conditions. The internal fluid flow has been assumed as an incompressible flow which simplifies the solution process.

In real situations, the Navier-Stokes equations are nonlinear partial differential equations, which can be challenging. Especially in the cases of turbulence, the convective acceleration along with the changes in velocity over position results in nonlinearity and solving the Navier-Stokes equations becomes extremely difficult. It is still believed that turbulence can be described properly by Navier-Stokes equations with supplemental equations and boundary conditions, just as with laminar flow. Generally, a finer mesh would give a more stable solution. However, it costs more computational time. In some cases, e.g. 1-dimentional flow and Stokes flow, the Navier-Stokes equations can be simplified to a linear one.

1.4 Electromagnetic Levitation

1.4.1 Electromagnetic Levitation Facility

In experiments measuring thermophysical properties like viscosity, density, and thermal conductivity, the interaction between sample and devices cannot be neglected. To obtain more precise measurements, eliminating the interference created by the facilities on experiments is one

of the best choices. For molten metals, the containerless measurement can be obtained by electromagnetic levitation (EML). This noninvasive technique has been applied in other areas, such as processing reactive metals and undercooled melt.

The conventional ground-based electromagnetic levitation facility (EML) is composed of two coil systems (Figure 1.1), providing positioning force and heating power. The former one, Lorentz force, which is used to levitate the sample is generated by the interaction of induced current and external magnetic field. At the same time, the eddy currents are generated by mutual inductance in the surface of the sample due to the alternating current in the heating coil system. As long as the current is large enough, the sample can be heated and melted easily by Joule heating. Then the heating field provides the power to keep the sample in liquid state during the experiments.

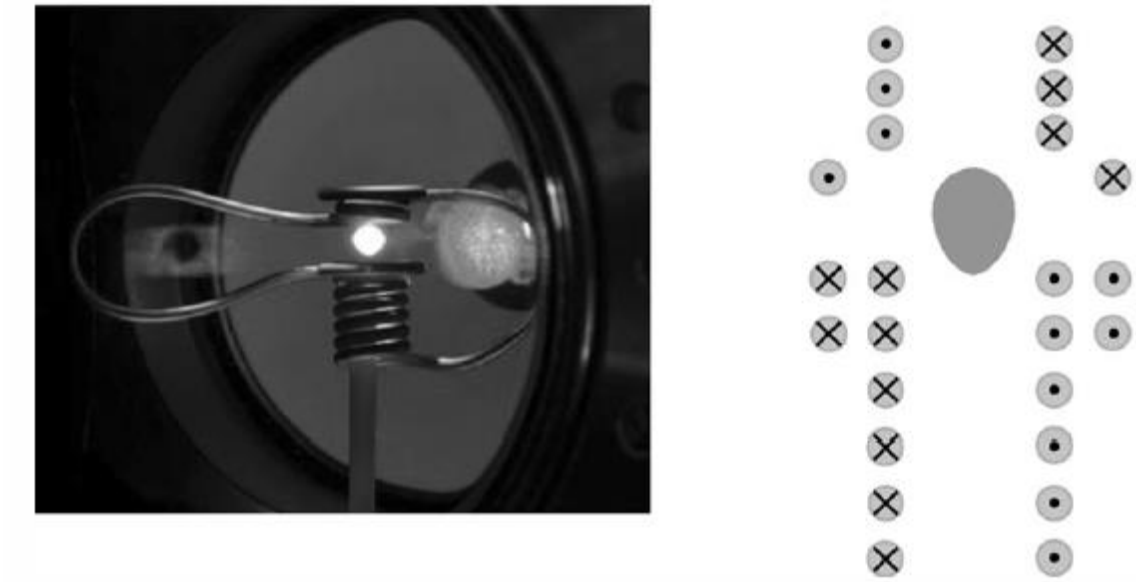

Figure 1.1: Ground-based electromagnetic levitation technique adopted by German Aerospace Center (DLR). The right pattern is the cross-sectional view of the coil system. The dot and cross indicate the current direction in coils. The sample is levitated in the center of the coil system and deformed due to gravity. [7]

To establish the internal convection of the opaque sample, tracer particles have been applied in EML experiments. In our observations, some aspects of the internal flow can be inferred from the motion and patterns of tracer particles on the droplet surface extracted from experiments record.

1.4.2 Electromagnetic Levitation in microgravity

On Earth, the electromagnetic force required to levitate an EML sample is so large that it drives strong internal flow in the liquid sample. The fluid flow tends to become turbulent due to high fluid densities as the viscosity decreases. The turbulence in the molten sample may influence nucleation kinetics, phase selection and interfere with thermophysical property measurements [1]. Therefore, in order to reduce the effect of electromagnetic forces, the experiments performed in microgravity are necessary, where the positioning forces required to counteract gravity are much smaller than those on Earth. Diagnostic tools and facilities have been designed for the Spacelab, such as “TEMPUS” (Figure 1.2). It has been adopted by space missions for thermal physical measurements like viscosity, surface tension and specific heat, and has also been used in processing undercooled states.

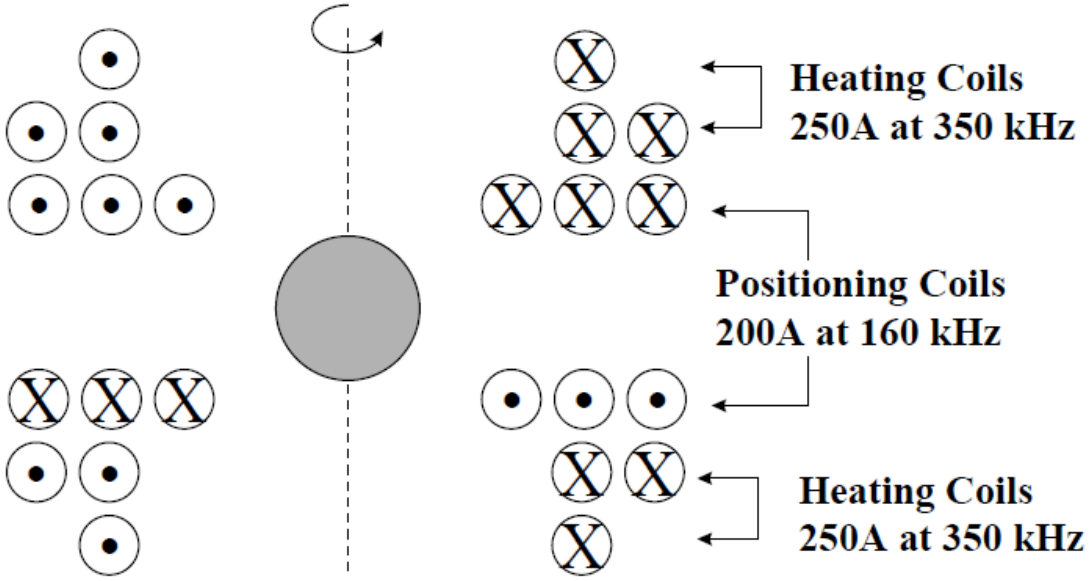

Figure 1.2: TEMPUS coil system. [21]

However, the coil set used for heating is inevitably more distant from the sample than the positioning coil set. As a result, the input power is decreased.

This efficiency shortage can be avoided by a new superposition levitation method--SUPOS, designed by the German Aerospace Center. The SUPOS employs only one coil system to generate both positioning force and heating power in microgravity [3]. In the SUPOS, the coils and condensers have been rearranged to create two independent oscillatory circuits to levitate and heat the sample at the same time [3]. To minimize the thermal effect of the positioning current and the electromagnetic force generated by the heating current, two coil arrangements have been designed: one of them is applied in this work. (Figure 1.3)

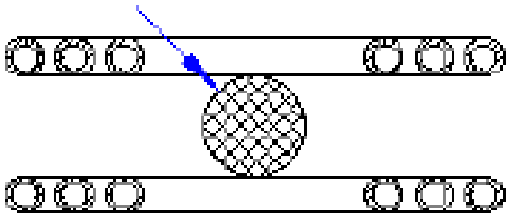

Figure 1.3: Cutaway of SUPOS coil system with the sample in the center. The arrow indicates the equilibrium position of the droplet. Copper tubes containing flowing water cover the coils to cool them down. [3]

Between the sample and coils is the sample holder made out of a combination of high performance ceramics and refractory alloys in high temperature. The sample holder not only serves as a sample transport container but it also provides protection to the coil system and facility chamber in case the liquid sample gets out of the control of the positioning force. (Figure 1.4)

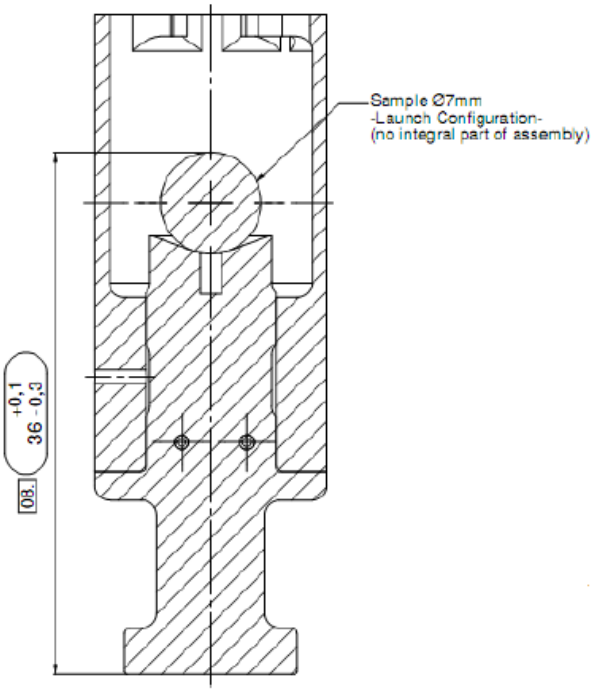

Figure 1.4: Sample holder. The arrow indicates the equilibrium position of the sample. [4]

Both the Lorentz force used to levitate the sample and induced heating power are related to the density of the magnetic field:

$$\mathrm{B}(\mathrm{x},\mathrm{t}) = B_0(x)\sin(\omega t) \tag{1.3}$$

$$F_L \propto -\nabla B^2 \propto I^2 \tag{1.4}$$

$$P_i \propto B_0^2 \propto I^2 \tag{1.5}$$

Where B is magnetic field density; F is Lorentz force; I is current in coil set; and P is induced power.

In addition, to counteract the residual gravity, this Lorentz force also prevents the droplet from escaping out of the sample holder. The sample is kept in the center of the coil system, where the magnetic density is weakest, to reduce the thermal influence of the positioning current.

1.5 Solidification

1.5.1 Solidification background

In material processing, solidification is a transformation of molten metals from a liquid to solid state. For example, in casting, molten metal is poured into the mold to cool and solidify into a certain shape. For pure metals, solidification occurs at a constant temperature, which is called the freezing point or melting point. The figure 1.5 shows how the process occurs over time. This is called a cooling curve. The plateau gives the solidification time from when freezing begins to when freezing is completed. Before and after the plateau the curves show the cooling process as a liquid and as a solid. During cooling and solidification, the latent heat of the molten metals is released to the surrounding environment. Over the curve, the cooling and solidification rate depends on the heat transfer and the thermal properties of metal.

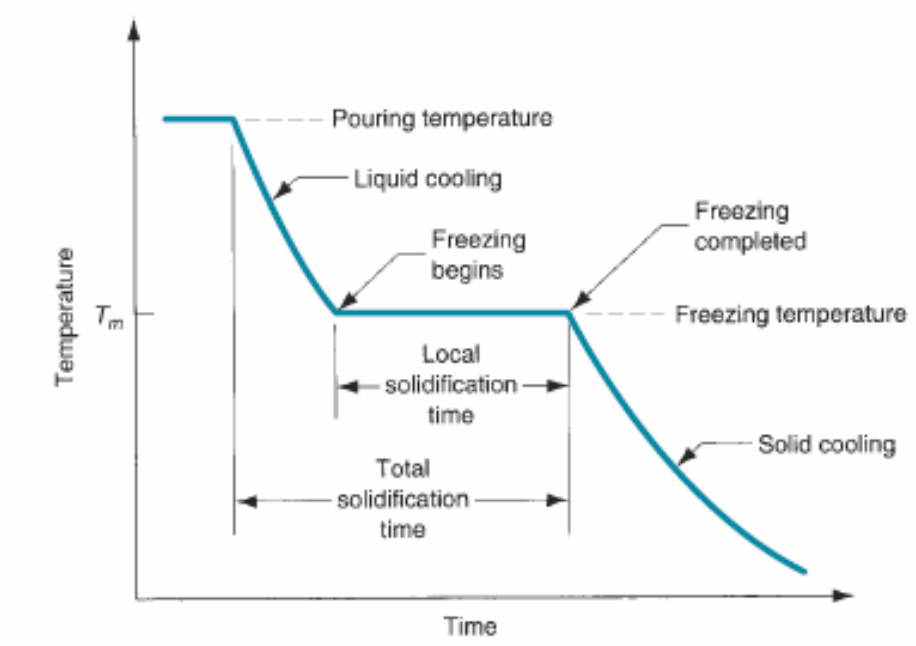

Figure 1.5: Cooling curve of a pure metal. [9]

Dendritic growth occurs during the freezing process. In solidification, the metallic grain is formed continuously and grows in a direction away from the heat transfer. Needles of solid metal are formed by the growth of grains, and then enlarged to form lateral branches, each growing at right angles to the previous one. The dendritic structure is just like a tree; new solid metal is deposited onto the dendrites to fill in the structure continually until the freezing process complete. Due to the dendritic growth, the preferred orientation of grains is coarse and toward the center of the casting. The figure 1.6 illustrates the grains clearly.

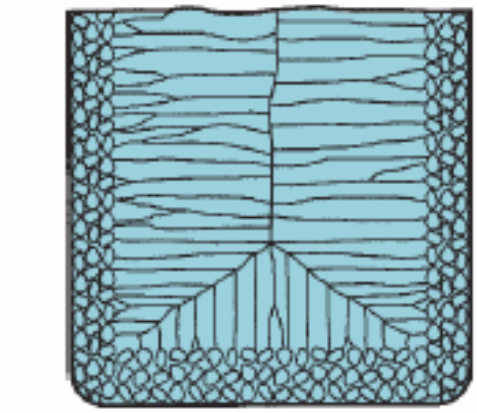

Figure 1.6: The grain structure of pure metal during casting. Small grains grow randomly near the wall while large columnar grains grow towards the center of the casting. [9]

The solidification process of alloys is different from that of pure metals. Instead of freezing at a constant temperature, alloys freeze over a temperature range and are affected by the particular composition. In the phase diagram--Figure 1.7 Left one, each cooling curve corresponds to a specific composition and the curve—Figure 1.7 Right one, is for 50%Ni-50%Cu. For alloys, the freezing process begins at the point of intersection of liquidus and composition, and ends at the point of intersection of solidus and composition in phase diagram. The alloy's freezing process is similar to that of pure metals in that there is also dendritic growth in solidification of alloys. The grains grow to form dendrites, developing away from the solid formed previously. In the phase

diagram, a new area named the mushy zone is generated between the liquid and solid solutions, and in the mushy zone both molten and solid metal exist. The nature of the mushy zone is established by dendritic growth due to the temperature transfer between liquidus and solidus. Eventually the dendrite structures can trap liquid metals to form a matrix that takes on a soft consistency. For different alloy systems and freezing conditions, the mushy zone may be relatively narrow or wide, even occupying most of the casting. As the heat transfers out of the molten metal to the surroundings, the liquid trapped in the dendrite structures solidifies gradually and is deposited on the branches until the temperature reaches the solidus of that particular alloy composition, which means the solidification process is complete.

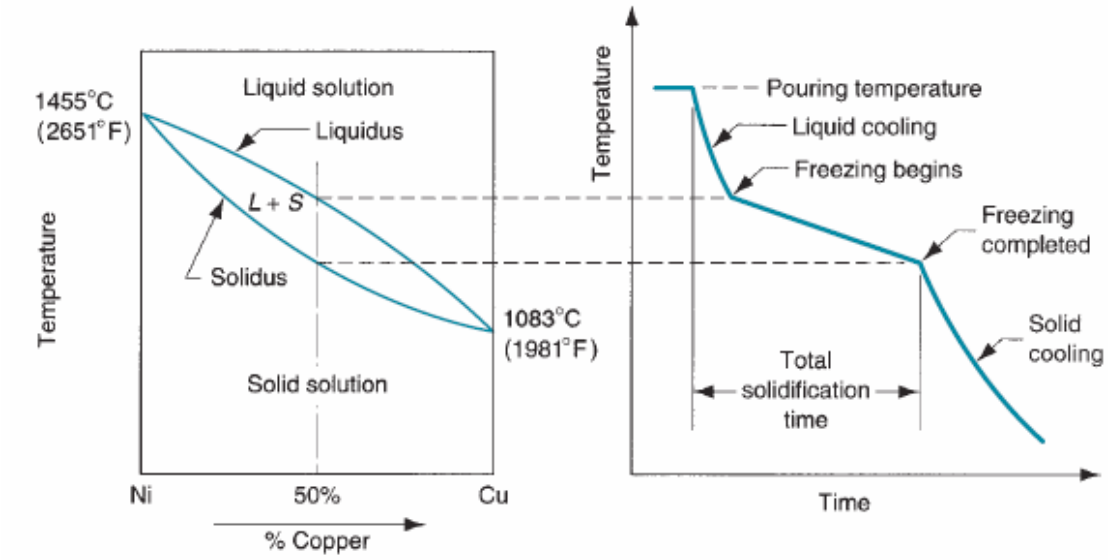

Figure 1.7: Left-Phase diagram of Cu-Ni alloy system; Right-Cooling curve of 50%Ni-50%Cu corresponding to the left phase diagram of casting. [9]

The microstructure of a certain alloy is directly related to the solidification process, and the mechanical properties of the alloy depend on the microstructure. The figures 1.8 shows two different microstructures of a Fe-Cr-Ni alloy system. The upper portion gives a “tree-like” dendrite microstructure, which can be found in the ferritic phase generated by the primary

transformation of a Fe-Cr-Ni alloy. In this dendritic geometry, the primary arms looks like the trunk of the tree and the secondary arms like the branches of the tree. The lower potion shows microstructure generated by double recalescence, which means the alloy solidifies to the metastable ferrite phase at first and ultimately transforms to a stable austenite phase. This results in fine equiaxed grains. The "tree-like" structure has been broken up by the secondary transformation.

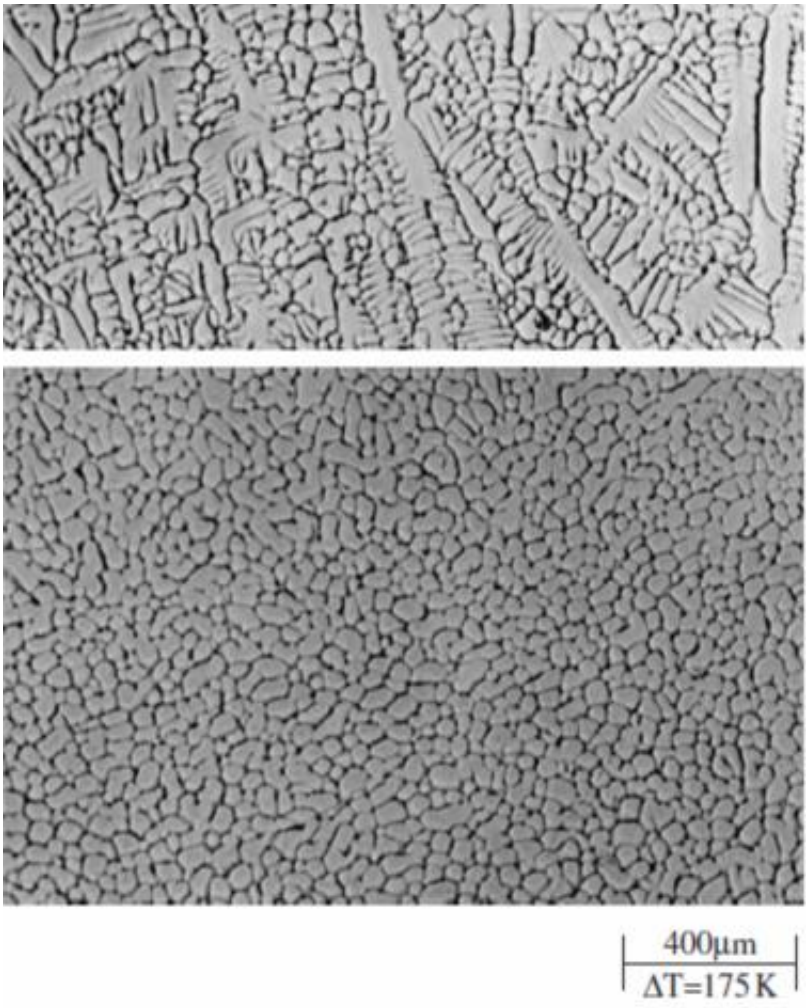

Figure 1.8: Microstructures of Fe-Cr-Ni alloy after solidification. Upper: Dendritic structure generated by single recalescence. Lower: Fine and equiaxed structure generated by double recalescence. [11]

Crystallographic texturing which is created by dendritic solidification leads to defects like shrinkage cavities and cause hot cracking, reduction of corrosion resistance and diminished toughness. The dendritic microstructure should be eliminated as much as possible in industrial applications, which can be achieved by double recalescence. The result is that the dendritic microstructure generated by the primary transformation can be eliminated and fine equiaxed grain structure will replace the "tree-like" geometry to yield more favorable mechanical properties.

1.5.2 Solidification of Fe-Cr-Ni alloy

The solidification process of Fe-Cr-Ni stainless steels is a good example. In short, to prevent dendrites from growing, the undercooled molten alloy should solidify to a BCC metastable phase first, and then transfer to the FCC stable phase at the end. This two-step transformation process is termed double recalescence.

The undercooling process means: certain molten alloy can stay in liquid state even when cooled to a temperature below the melting point.

There are two ways for the Fe-Cr-Ni alloy to transform from undercooled liquid to solid state, either by single or double recalescence. The Figure 1.9 shows a phase diagram for a Fe-Cr-Ni alloy which shows two paths clearly. The composition is of 72 wt.-% Fe isopleth. From left to the right side, the wt% Cr is increasing and the wt% Ni is decreasing. On the left part of the diagram, the stable solidified state is FCC, and on the right part, BCC. In Hanlon's previous work [10], the alloys tested were Fe-12 wt.% Cr-14wt.% Ni, located in FCC region. In this region, the upper dotted line implies the extension of the solidius and liquidus line below the eutectic point, called the metastable solidus line. Along the composition line, when the temperature of the undercooled alloy is below the intersection of composition and the metastable solidus line, the molten alloy may solidify to a BCC metastable phase first and then transform to the FCC stable phase.

Theoretically, if the metastable phase is generated throughout the alloy completely before the stable phase formed, the final microstructure will be composed of same size and shape grains, which will yield a more strengthened alloy.

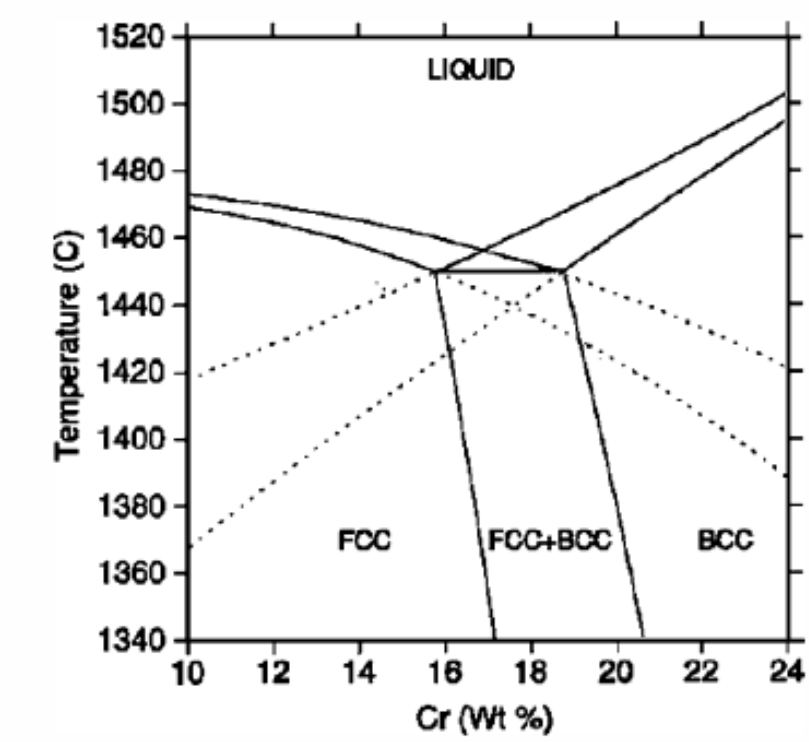

Figure 1.9: Phase diagram of Fe-Cr-Ni alloy on 72% Fe isopleth. [11]

The lifetime of a metastable phase is called the "delay time", and plays an important role in the final microstructure. If the delay time is not long enough for the molten alloys to complete primary nucleation before the final transformation begins, the remaining part of the molten alloys will solidify to the FCC stable phase directly, forming a crystalline structure.

In experiments with undercooling less than 150 degrees C, the FCC stable phase is formed more quickly than the BCC metastable phase, although the formation of the BCC phase started first. The process of FCC stable phase formation ultimately overtakes and exceeds the BCC one. As a result, the solid alloy is composed of two different microstructures. As shown in the figure 1.10,

the top region, created by 2-step solidification, is of refined grains with similar size and shape, offering more grain boundaries. In contrast, an obvious dendritic structure can be found on the bottom region, where the molten alloys solidified to austenite phases directly.

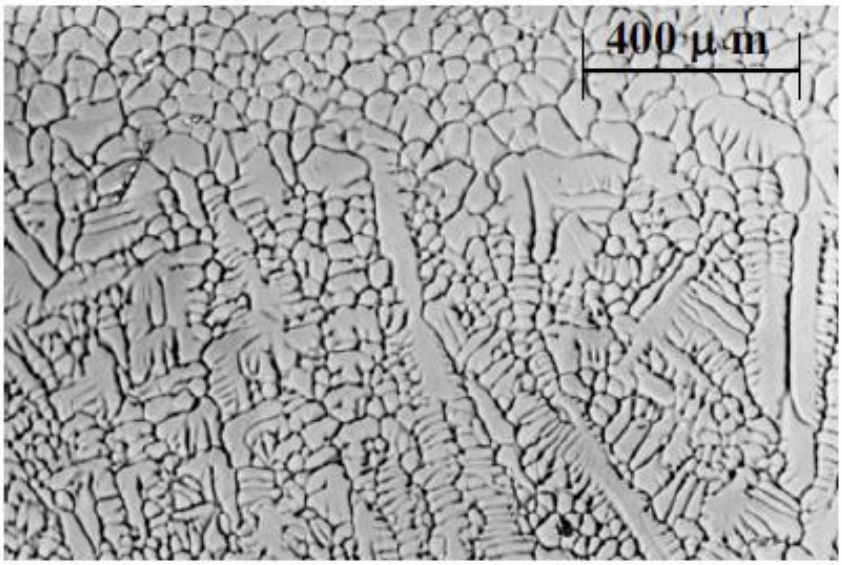

Figure 1.10: Microstructure of Fe-Cr-Ni system. The top portion consisted of fine grains generated by double recalescence, while the dendritic structure exists in the bottom portion due to single recalescence. [10]

1.5.3 Convection in solidification process

A hypothesis has been tested by Hanlon's previous work that delay time is strongly related to the convective velocities obtained from solidification experiments. [12] The simulation result shows that mechanical damage of the microstructure may be caused by the induced convective flow. With strong enough convective velocities, the induced fluid flow can damage the growing dendrites in primary nucleation. The figure 1.11 and 1.12 show this mechanical damage as a collision of two secondary adjacent arms as a result of the primary dendrite deflection. These

points of collision give rise to low-angle boundaries, which cause the premature transformation to the stable phase. In figure 1.11, there are no collisions to set off the transformation to stable phase. Figure 1.12 shows the collision of secondary arms on the deflected dendrites caused by strong internal convection.

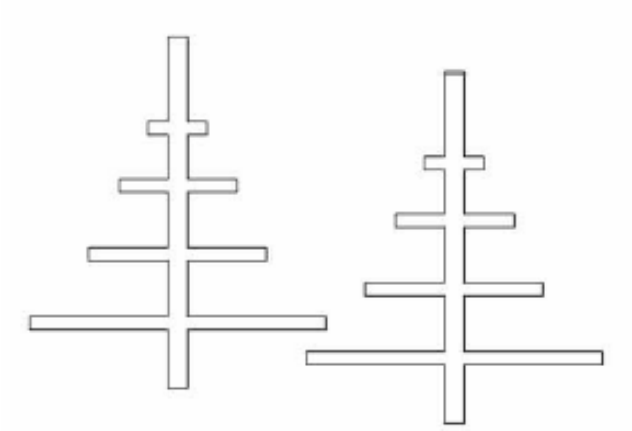

Figure 1.11: Dendrites growing in slow convection without collision. [12]

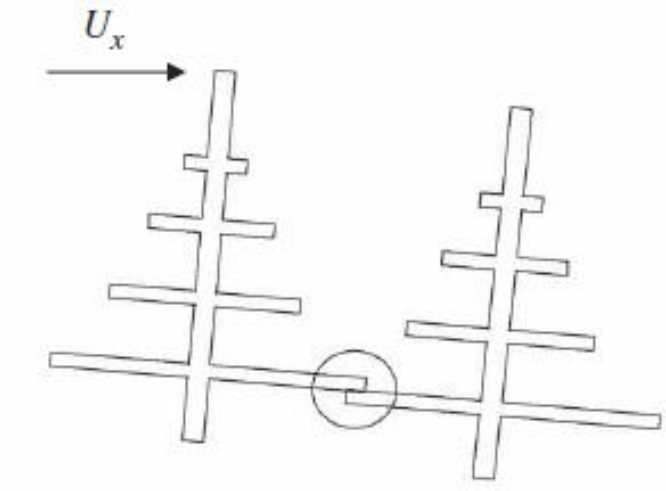

Figure 1.12: Collision is caused by the strong convection. The arrow shows the direction of flow velocity. [12]

Therefore, the convective velocity in the liquid metals or alloys is significant for microstructures generated by solidification. In this work, different numerical models have been tested to evaluate the fluid flow velocity at turbulent transition. Thus, in following studies it will be easier to choose the appropriate model to numerically evaluate the corresponding convection: laminar, turbulence and turbulent transition. It will also save much time on subsequent research.

The containerless method has been applied in experiments studying internal convection in solidification. The techniques include both electromagnetic levitation (EML) and electrostatic levitation (ESL).

In electromagnetic levitation (EML), the samples of Fe-Cr-Ni alloy can be levitated and melted by an electromagnetic fields generated by alternating current. The sample adopted in EML is a sphere with a diameter of 7mm. The induced current in the sample interacts with the external electromagnetic field and produces both the Lorentz force to levitate the sample and the heat to melt it. The internal magnetohydrodynamic convection appears when the sample becomes fully melted. The magnetohydrodynamic models have been built to quantify the induced flow in the molten sample. Reference to the previous work on ground-based EML [2]shows that the velocities of internal flow of droplets are on the order of 0.32m/s, which is turbulence. That's because the sample needs a large Lorentz force to counteract gravity, leading to a strong internal flow. The only velocities of internal convection that can be tested in 1-g EML are of turbulent flow, which really limits material scientists.

Electrostatic levitation (ESL) is the other containerless technique used in the experiments. To make sure the Fe-Cr-Ni samples adopted have the same composition as the ones used in EML, the scientists remove a part of these samples and use them as the new samples for ESL. [19] These are 2mm in diameter. Electrodes produce an electrostatic force to levitate the sample. The light source provides a photoelectric effect on the sample to keep it charged [20] while the sample

is heated and melted by lasers. The thermal gradients along the droplet sample cause Marangoni convection, which drives the internal flow at low velocities. Since the experiments occur in vacuum, there is no heat loss due to convection or conduction. The convective velocity is on the order of 0.04m/s of ground-based ESL flow, which is laminar. [21]

The figure 1.13 shows the big difference in delay time between the ground-based EML and ESL experiments [19]. Although the samples applied in EML and ESL testing share the same composition Fe-12Cr-16Ni, the delay times obtained from ESL are almost two orders of magnitude greater than from EML. Several hypotheses attempting to explain the difference in delay time have been disproved by the work of reference [22, 23]. The hypothesis that the lifetime of the metastable phase is directly related to the internal fluid flows is convincing. [23.24]

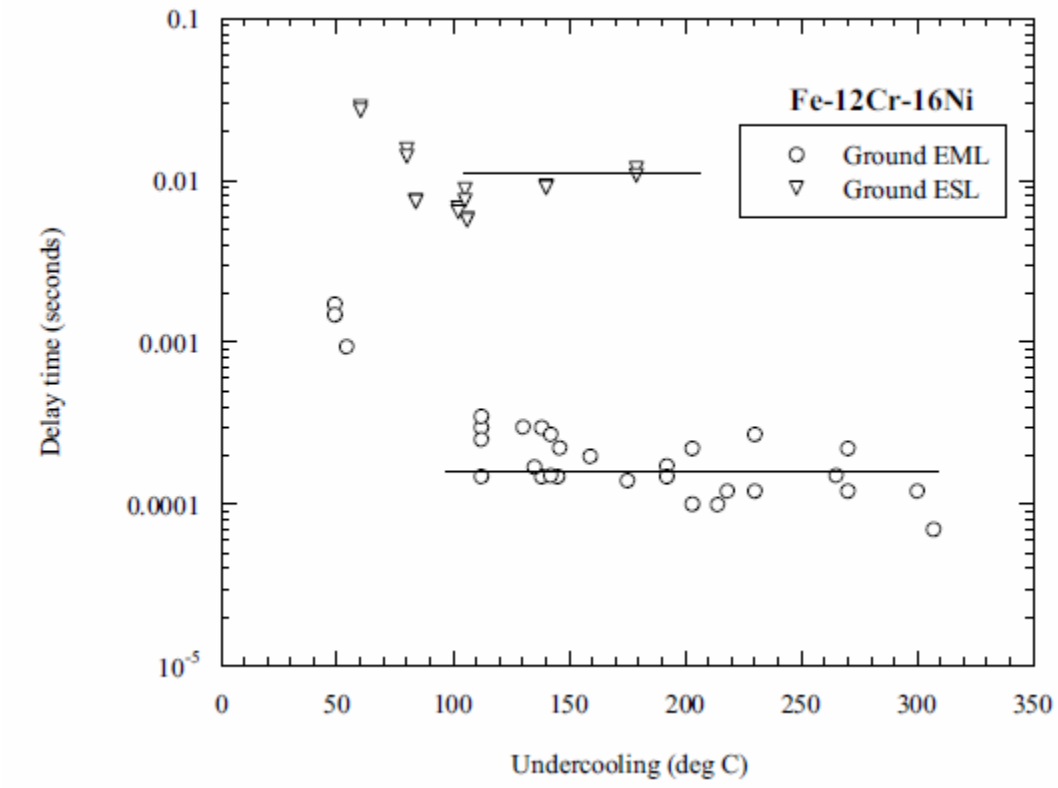

Figure 1.13: Delay times of 1-g EML & ESL experiments. [19]

Previous works have identified the velocity of turbulent flow in 1-g EML as 0.32m/s [2], which means only high-velocity turbulent flow can be obtained from ground-based EML. The strong convection observed in samples is induced by the strong positioning force required to counteract gravity. However, in ground-based ESL, only low-velocity laminar flow is found on the order of 0.04m/s, as a result of the Marangoni convection. Figure 1.14 and Figure 1.15 gives the velocity and Reynolds number ranges obtained from ground-based EML and ESL experiments. There is an obvious gap between the two ranges, which means the full range of convection is not accessible in ground-based experiments. But the gap can be fixed by the microgravity experiments. The section 1.4.2 will give more details.

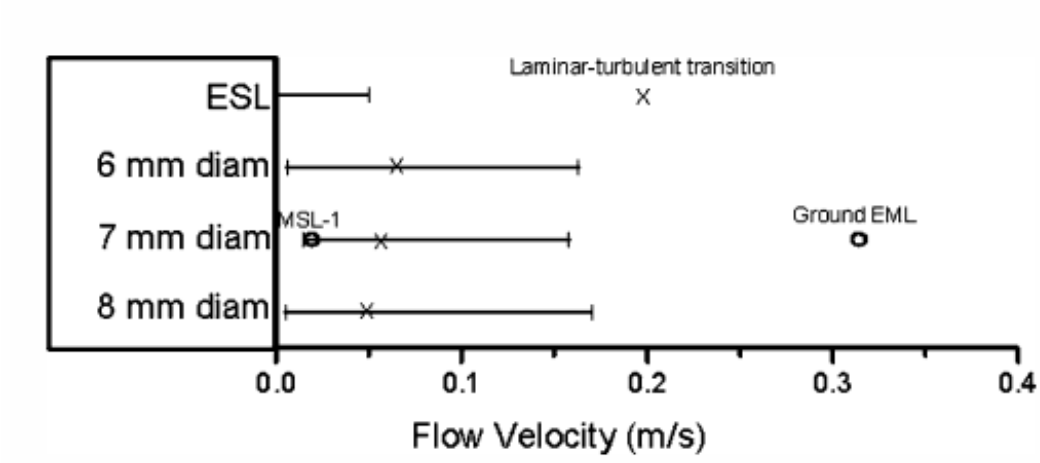

Figure 1.14: Convection range obtained from 1-g EML, ESL and microgravity EML in terms of convective velocity. The circles show the convection accessible through 1-g EML and MSL-1 EML. [2]

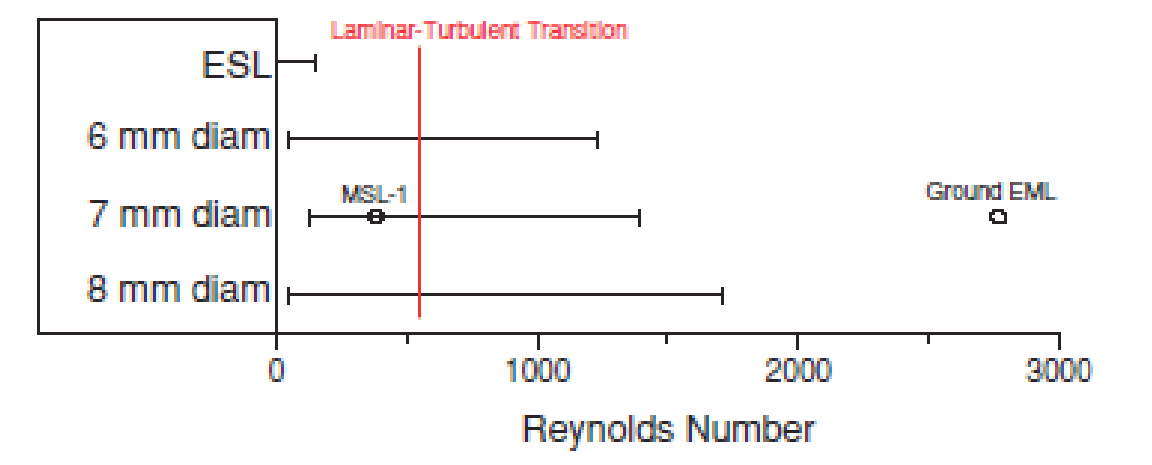

Figure 1.15: The Reynolds number obtained from 1-g EML, ESL and microgravity EML. The circle gives the convection of ground EML and MSL-1 experiments. [2]

The microgravity electromagnetic levitation experiments have been conducted recently in order to fix the existing gap in convective velocity range. Microgravity EML provides a good chance to obtain the data in this gap, because the strong positioning forces required in ground-based EML are not needed in space. The velocities tested in microgravity EML can be as moderate as low velocity laminar. Meanwhile, large forces can be applied too. The high velocity turbulence are also available in space. The velocities gap, which is not accessible on Earth, can be covered by the microgravity EML experiments.

1.5.4 Experiments on parabolic flights

In this work, parabolic flight experiments with clear phenomena of laminar-turbulent transition were selected. In Hyers' work [1], the Reynolds number at laminar-turbulent transition has been estimated as 600 for a spherical sample. In this study, a new geometry is adopted: ellipsoid, instead of a sphere sample. Moreover, new models have been developed. Since the convection velocity crucially affects material properties through solidification, the numerical models from

this work can be adopted by simulation based on the situation—laminar, turbulent or turbulent transition—to calculate the magnitude of the convective velocity. Thus, the solidification process can be learned and controlled to generate strengthened microstructures. The computational time cost will be reduced too.

1.6 Magnetohydrodynamic flow in containerless levitation experiments

In many applications of containerless levitation, (e.g. measurements of viscosity) the stability of the internal flow is more important than the absolute magnitude of the flow velocity. On the other hand, the accurate magnitude of convective velocity is crucial in solidification.

1.6.1 Convection in experiments

The numerical models tested by this work can be used to evaluate the fluid flow velocity in molten alloys or metals during solidification, so that strengthened materials can be achieved by controlling the convection in solidification.

In order to ensure the accuracy of the thermophysical properties measurements, the fluid flow in the sample should be controlled in a certain flow condition. Containerless methods eliminate any chance of chemical reaction between the sample and test facilities. However, even in containerless methods results are often critically affected by the internal convection of the samples. For example, in measurements of viscosity, the test droplet is excited by an oscillating force field near the natural frequency of the sample which then dampens out freely. The viscosity can be estimated using the measured decay time. If the internal flow is turbulent, a considerable portion of the energy of the oscillating droplet should be dissipated by the turbulent eddies so that the decay time becomes much shorter, resulting in too large a value of viscosity. On the other hand, in measurements of heat capacity turbulent mixing reduces the temperature gradient in the

sample. This means the heat capacity can be measured more effectively, especially when a material has a high Biot number. In short, the status of the internal convection can either facilitate or jeopardize the property measurements. Therefore, it is important to identify the convection state during the measurements of thermophysical properties of molten metals and alloys.

From this study of turbulent transition, the upper limitation of laminar flow and the lower one of turbulence can be more clearly measured. Thus, the results of this study can be used to improve the measurements design in order to obtain thermophysical properties accurately. For example, the figure 1.16 shows the uncertainty from the thermophysical properties measurements of Zr due to the convection [29]. The values in shadow means turbulent transition occurred, which is a large portion to the whole tests.

Tm – 300 K	Heater V [V]			
Positioner V [V]	0	0.2	0.4	0.6
6	361	413	490	582
7	395	427	500	576
8	421	449	511	577
9	451	476	532	598
10	487	506	555	622

Tm – 200 K	Heater V [V]			
Positioner V [V]	0	0.2	0.4	0.6
6	390	447	530	630
7	427	462	541	624
8	456	486	553	624
9	487	515	576	647
10	527	548	601	673

Tm – 100 K	Heater V [V]			
Positioner V [V]	0	0.2	0.4	0.6
6	425	487	578	686
7	466	503	590	680
8	496	530	603	680
9	531	561	627	705
10	574	597	654	734

Tm	Heater V [V]			
Positioner V [V]	0	0.2	0.4	0.6
6	468	535	635	755
7	512	553	649	747
8	546	583	663	748
9	584	617	690	775
10	632	656	720	807

Tm + 100 K	Heater V [V]			
Positioner V [V]	0	0.2	0.4	0.6
6	520	595	706	839
7	569	615	721	831
8	607	648	737	832
9	650	686	767	862
10	702	730	800	897

Tm + 200 K	Heater V [V]			
Positioner V [V]	0	0.2	0.4	0.6
6	587	671	796	946
7	642	694	813	937
8	684	730	831	938
9	732	773	865	972
10	792	823	902	1011

Laminar (Re < 500) Transition (500 < Re < 700) Turbulent (Re > 700)

Figure 1.16: Convection in reference sample Zr. [29]

1.6.2 Numerical modelling of magnetohydrodynamic

The magnetohydrodynamic flow in EML droplets is driven by Lorentz forces and governed by the Navier-Stokes equations (1.1) (1.2) with the boundary conditions—(1.6) for laminar flow; turbulent flow requires both (1.6) and (1.7).

$$u_r^*\big|_{r^*=1} = \tau^* \cdot i_t\big|_{r^*=1} = 0 \tag{1.6}$$

$$\left.\frac{\partial k^*}{\partial r^*}\right|_{r^*=1} = \left.\frac{\partial \varepsilon^*}{\partial r^*}\right|_{r^*=1} = 0 \tag{1.7}$$

Where k is turbulent kinetic energy; ϵ is turbulent dissipation.

The Reynolds number can be expressed as:

$$\mathrm{Re} = \frac{\rho u D}{\mu} \tag{1.8}$$

Where Re is Reynolds number; ρ is density; U is velocity; D is diameter and μ is viscosity.

The magnetic force is generated by the interaction of inducted current and the positioning electromagnetic field. [2]

A commercial finite element code, named FIDAP, has been adopted by the simulations of numerical modelling. The geometry is a 2-D axisymmetric sphere and the force which drives the flow is calculated by a subroutine separately.

The results show that the modelling of flows near the laminar-turbulent transition is pretty difficult. According to the work of Hyers *et al.* [1], the laminar-turbulent transition occurs when the Reynolds number reaches up to 600 in the molten sample of EML experiments. The work of Berry *et al.* shows that the renormalization group method (RNG) variation of $k-\varepsilon$ performs best on the modelling of turbulent internal flow in EML droplets. [7]

For the TEMPUS coil set, the simulation results by Hyers *et al.* provided two typical flow patterns of FeCrNi alloy—positioner-dominated (Figure 1.17) and heater-dominated internal convection (Figure 1.18). Both patterns are mirror symmetric and axisymmetric. There are four loops on the pattern of positioner-dominated flow in droplets with low Reynolds numbers. The two loops near the poles keep shrinking as the Reynolds number increases and disappears finally. The heater-dominated flow pattern is different from the positioner-dominated one, consisting of only two loops. As a result of opposite flow directions, the equatorial loops driven by positioning field can be weakened by the ones driven by the heating field. Therefore, the minimum velocity of flow can be obtained when the forces generated by the two fields are balanced.

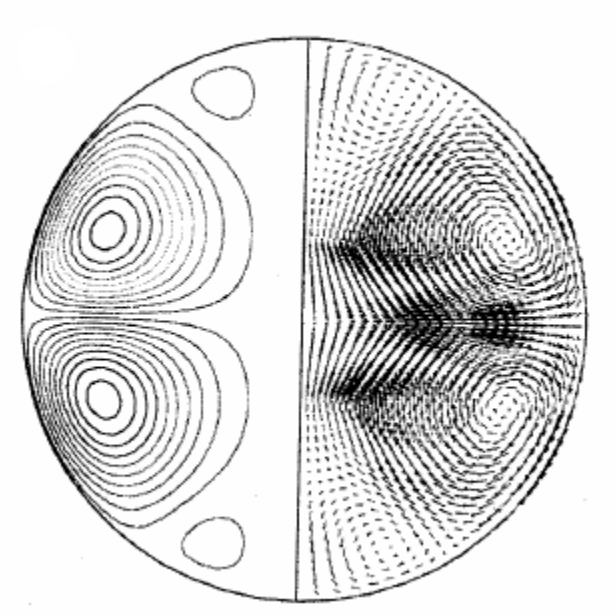

Figure 1.17: Positioner-dominated flow patterns of FeCrNi alloy—streamline (Left) and velocity field (Right). Positioner current is 150A and heater current is 0A. [2]

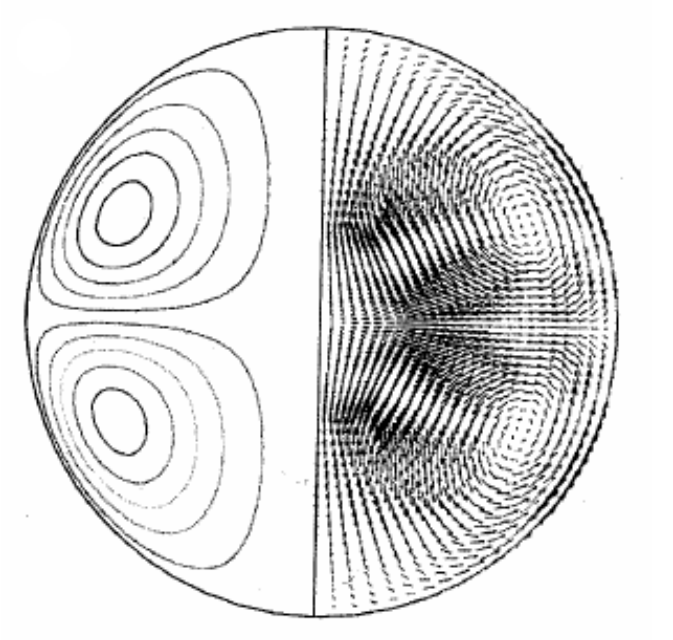

Figure 1.18: Heater-dominated flow patterns of FeCrNi alloy—streamline (Left) and velocity field (Right). Positioner current is 150A and heater current is 40A. [2]

The convections from EML (Electromagnetically levitated) and ESL (Electrostatically levitated) droplets share the same governing equations and boundary conditions. In addition to the heater-dominated flow, the positioning force of EML can drive the flow dominantly too. In contrast, the Marangoni convection in ESL droplets is driven by the temperature gradient provided by the heating laser, which is independent of the positioning facility. Moreover, the ESL droplet problems share the same numerical solution method with EML ones. FIDAP has been adopted to solve the problems on a 2-D axisymmetric spherical geometry and the heating process can be expressed by a boundary condition subroutine. The figure 1.19 shows the simulation results of flow velocity for a $Fe_{72}Cr_{12}Ni_6$ case.

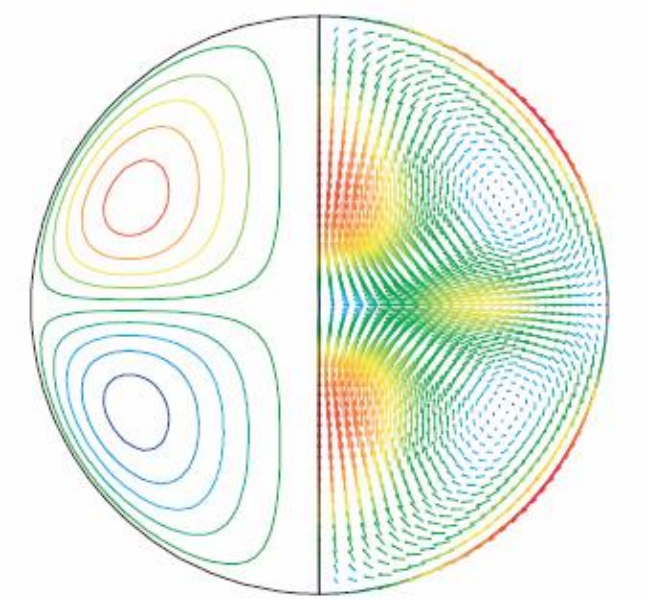

Figure 1.19: The velocity field and streamlines obtained from a 1-g ESL $Fe_{72}Cr_{12}Ni_6$ droplet. The maximum velocity is 5.6 cm/s. [6]

In short, since the velocity and temperature distributions cannot be measured directly from the droplets in EML or ESL experiments, the numerical modelling method is necessary for the quantification of convection and thermal conditions. The simulation results (Figures 1.14 and 1.15) provide a clear description of the velocity range covered by various systems. The range of convective velocity accessible by ground-based experiments is very narrow. The Reynolds number that can be achieved by 1-g ESL is less than 110, with a velocity of 4.4 cm/s, which does not reach up to the laminar-turbulent transition. Meanwhile, ground EML results in too big a Reynolds number, 2800, in which turbulence has already developed. The line segments corresponding to various sample sizes (6, 7 and 8mm in diameter) indicate the velocity ranges obtained in microgravity EML. It is observably wider than that in ground-based testing. [2]

In ground-based EML tests, the range of sample size is narrowed by the operating conditions in order to ensure a stable levitation. As a result, a limitation of convective velocity cannot be avoided. In ESL tests, the dominating Marangoni convection is driven by the surface tension

gradients caused by the temperature gradients, which are independent of operating conditions. The Marangoni convection in the ESL can reach up to 6 cm/sec and almost disappear when the heating laser is turned off.

In microgravity EML testing, the convective velocity is downwardly limited by the positioning force required to counteract gravity and control the sample in the equilibrium position, and upwardly limited by the heating-induced convection in the sample.

1.6.3 Laminar-turbulent transition in experiments

The tracer particles have been adopted by the microgravity EML experiments to give a view of the internal flow via their movements on the levitated liquid sample surface. With the help of the tracer particles, the time of the turbulent transition can be determined. Moreover, the corresponding Reynolds number can be obtained from the numerical evaluation.

When the levitated sample is heated until totally melted, the tracer particles will accumulate on the band of the equator indicating that the internal convection is steady laminar. The corresponding flow pattern can be predicted by the numerical model as the figure 1.18. If the viscosity of the sample is strongly dependent on temperature and the sample is continually heated, the internal flow will keep accelerating due to the decreasing viscosity. At this point the internal flow becomes unstable and eventually fully turbulent. According to Hyers' work, it happens at the Reynolds number of 600.

1.7 Viscosity

1.7.1 Viscosity background

Viscosity is the ability of fluid to resist the shear stress or tensile stress of deformation. Particles next to each other in fluids may move with different velocities and the friction due to the movement is the leading cause of resistance. External force (e.g. pressure difference) is required to overcome the friction, and to keep the fluid moving. Because liquids consist of small molecules, the relationship between shear rate and shear stress can be expressed linearly: [25]

$$\tau_{zx} = -\mu \frac{dv_x}{dz} \tag{1.9}$$

Where τ_{zx} is shear stress and $\frac{dv_x}{dz}$ is velocity gradient.

All metals are regarded as Newtonian, so the relations above can be adopted. More complicated relations between shear stress and shear rate should be considered for large polymers and fluid mixtures.

1.7.2 Viscosity Measurement

The study of viscosity is essential for fluid dynamics and thermodynamics as well as in industrial areas like casting and welding. For example, in computational modeling of magnetohydrodynamic flow, the utility of the results depends on the accuracy of thermophysical properties like viscosity. And knowledge of viscosity is essential for the designation of a new alloy system, to predict the final performance of alloy.

It is difficult to measure the viscosity of molten metals or alloys by traditional measurement techniques due to the high temperature. Another difficulty is that the sample in liquid phase tends to be contaminated easily. Electrostatic levitation (ESL), as one kind of containerless method, has

been used by several groups [6,14] to measure the thermophysical properties of molten alloys. By electrostatic levitation furnace, the sample can be heated and melted by multiple laser heating beams without contacting any walls or gases, which eliminates contamination. This is an important advantage in testing corrosive materials, especially in liquid phase. It also means that the sample can be made stable enough to accomplish the measurement. Since the sample is positioned and heated by two independent systems and the electrostatic system does not generate any heat, a wide temperature range can be achieved. The levitated sample can be undercooled or superheated and sustain the state long enough to complete the measurement.

There were two kinds of sample holders: A wire cage of W-Re with SiC pedestal, and a cup-type holder of SiC. The cup holder acted as a shield to protect the levitated coils from being exposed to the strong evaporation sample.

In addition to the measurement of thermophysical properties in liquid alloys, the ESL facility has other applications too, like synthesizing new materials and the study of corrosive solids. For example, the tests of some materials (e.g. niobium, which has a very high melting temperature) can be accomplished by ESL for its containerless features.

The oscillating drop method has been applied in ESL to measure the viscosity and surface tension of levitated metal droplets. The measurement is based on the theory from Kelvin's work about the oscillations of viscous drops. [27] The viscosity μ can be obtained from a damping constant Γ derived by Kelvin:

$$\mu=\frac{\rho r_0^2}{5\tau} \tag{1.10}$$

where μ is viscosity; ρ is liquid density; r_0 is radius of the sample; and τ is damping time.

This equation (1.11) can be applied only for spherical droplets without the effect of external fields.

In this method, an oscillation of the molten sample to its equilibrium state is required. The levitated liquid sample is excited to oscillate at its natural frequency and then allowed to dampen freely. The damping time is determined by the viscosity of sample. [26] This method allows samples of even corrosive materials to be tested in a metastable undercooled state.

When the sample is positioned in the holder stably, it can be melted and overheated. Then the heating process is stopped by turning off the heating fields so that the sample can cool down by radiation. During the cooling cycle, the excitation current pulses in the heating coils generates a force to compress the sample laterally that the droplet is excited to oscillate. In the $Pd_{76}Cu_6Si_8$ case [18], the excitation force was generated every 50K until solidification completed. The radius of the sample can be observed by analyzing the video tape specifically. It turns out that the radius of the sample changes as a function of time. Both the damping constant and frequency can be obtained from the signal.

The oscillating drop method has also been applied in electromagnetic levitation (EML), including ground-based testing [31], parabolic flights [32,33], and on the space. [34,35]

The figure 1.20 shows the oscillation of a molten silver sample in the TEMPUS device under microgravity.

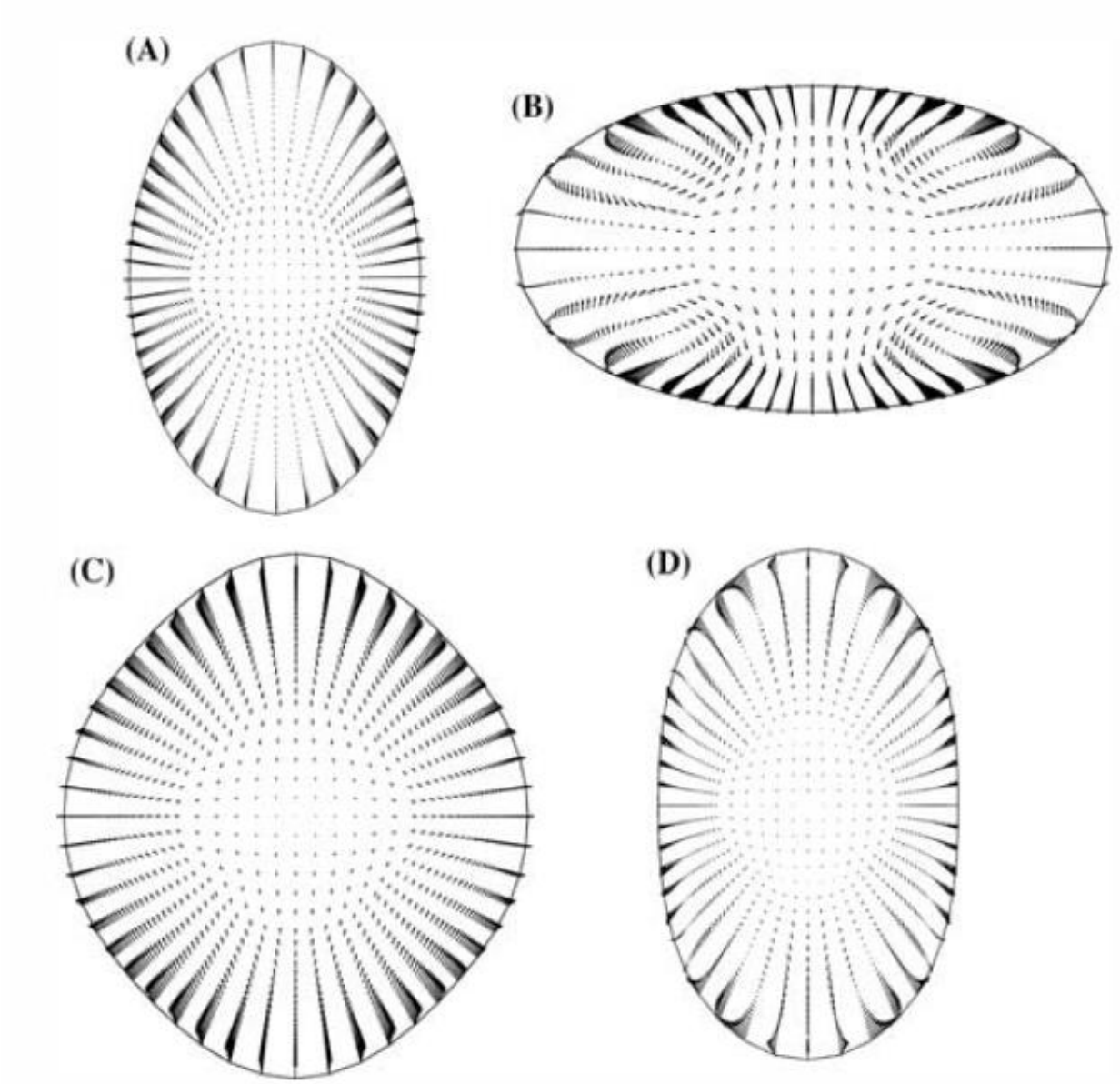

Figure 1.20: The oscillation process of silver measured by microgravity TEMPUS. [8]

1.7.3 Numerical evaluation of convection in viscosity measurement

Since electrostatic levitation is applied in a vacuum without current, there is no component tangential to the electric field of the levitated sample. Therefore, no electrohydrodynamic flow exists like the EML droplets. The Marangoni convection is the main internal convection in ESL droplets, which is caused by gradients in surface tension. The laser heating effect has been taken into account by computer modeling, which includes heat distribution and thermal radiation. Since the droplet was levitated in a vacuum, the heat loss due to conduction or convection can be neglected. The thermal gradients on the droplet's free surface are the main cause of surface tension gradients. The figure 1.21 shows the thermal profile of two droplets, with and without rotation.

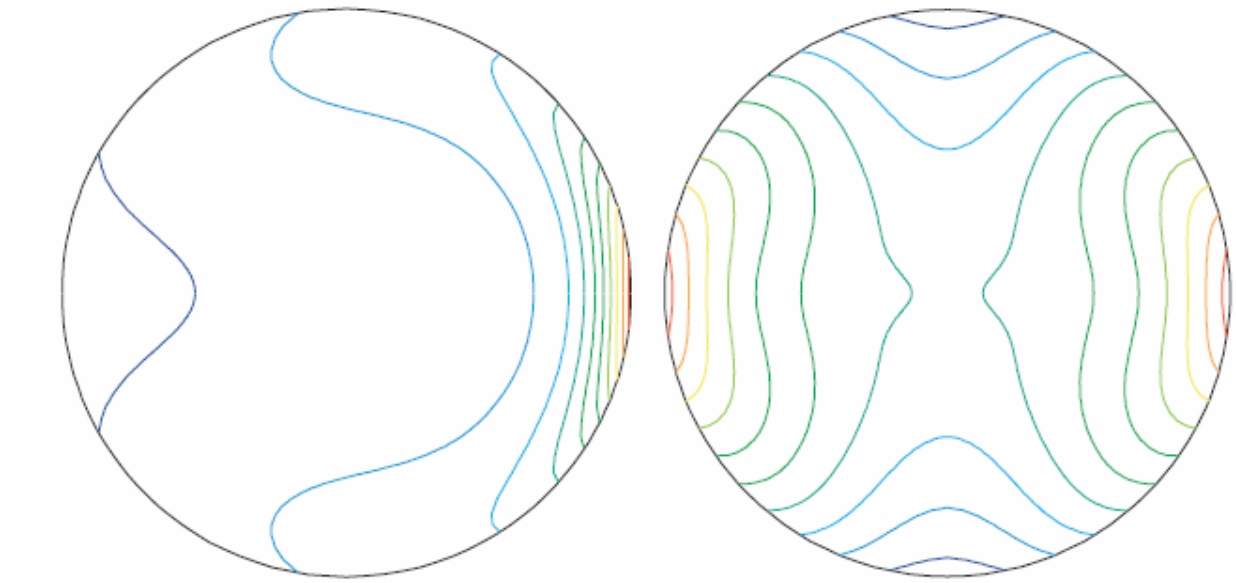

Figure 1.21: Temperature profiles in non-rotating (Left) and rotating (Right) samples of $Fe_{72}Cr_{12}Ni_{16}$ system. The maximum temperature difference is 29K (Left) and 6K (Right) respectively. [6]

Temperature gradients on droplets are directly related to the droplet rotation. If the sample is heated without rotation, the power absorbed by the droplet will concentrate in a very small area of

droplet surface, which is the main cause of a large gradient of temperature. The large Marangoni convection is directly related to the large temperature gradient. When the droplet rotates slowly, the laser power can be distributed along the track, which will indeed reduce both the temperature gradient on the droplet surface and Marangoni convection.

Marangoni convection in ESL droplets has been modelled by many groups. Navier-Stokes equations (1.1) (1.2) with relevant boundary conditions (1.6) (1.7) and energy equations have been adopted in computer modelling. For analytical models of creeping flow, see Bauer and Eidel's work [28] and for numerical models see Hyers' [2] and Li and Song's work [29]. The numerical one is more commonly adopted.

The ESL droplets of $Fe_{72}Cr_{12}Ni_{16}$ system have been numerical modeled by Hyers' et al. [6], in order to study the convection. The figures 1.22 show the calculation results.

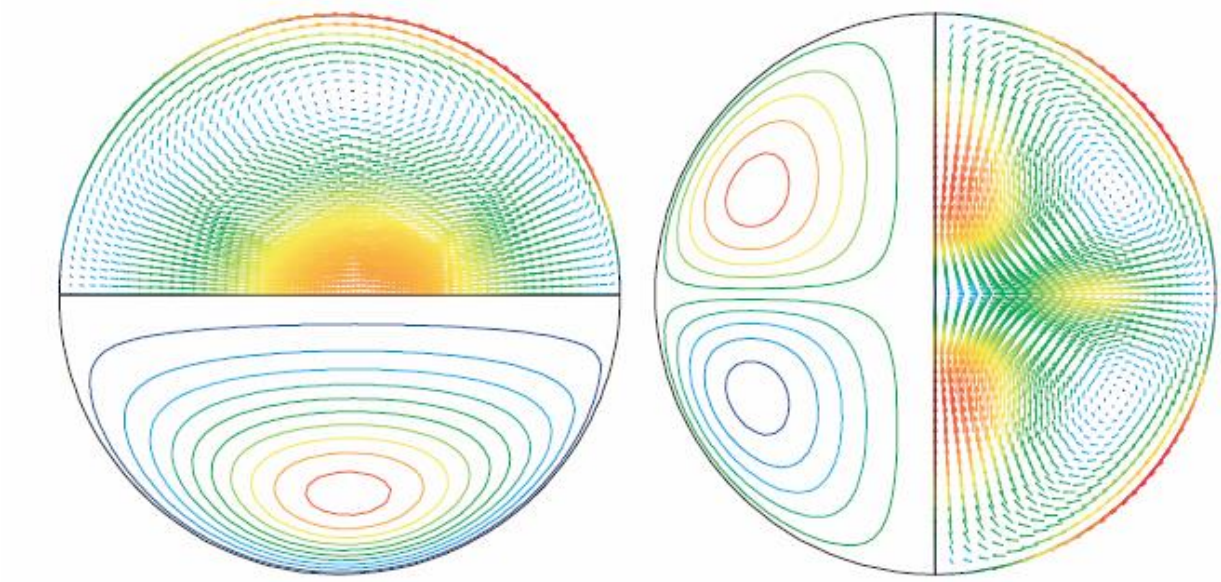

Figure 1.22: The velocity field and streamlines of non-rotating (Left) and rotating $Fe_{72}Cr_{12}Ni_{16}$ alloy droplet (Right). The maximum convective velocities are 13cm/s (Left) and 5.6 cm/s (Right) respectively. [6]

When measuring viscosity, the internal flow affects the results' accuracy. Internal turbulence can ruin the measurements completely by consuming the energy necessary for sustaining oscillation. Turbulence eddies are the main cause of energy dissipation, causing the droplet to stop oscillating earlier for lack of enough energy.

This study of laminar-turbulent transition can provide more information about high-velocity laminar, which will be a good reference for viscosity measurements designation.

1.8 Convection in surface tension measurements

Measurements of surface tension and viscosity share the same oscillating drop method of containerless processing. The levitated sample can be melted and oscillated in a force-free environment as a high-quality mechanical oscillator. The surface tension is related to the resonant frequency of the oscillatio.

The measurement of surface tension is affected by the internal fluid flow too. For example, an extra oscillation can be excited by the internal turbulence, which may reach such a large amplitude that a non-linear effect leads to the reduction of the measurement's precision. Moreover, the high velocity laminar flow causes extra oscillation too. For example, in ESL experiments, when the period of recirculation of the flow loops is comparable to that of oscillation, the amplitude can be enlarged due to the interaction of both flows. Therefore, internal convection in measurements of surface tension should be understood and under control.

Unlike clear laminar or developed turbulent flow, less is understood about laminar-turbulent transition. As the velocity of the fluid flow increases, the Reynolds number approaches the turbulence region and the fluid flow becomes unstable. In this situation, it is hard to define

whether the viscosity or surface tension measured is accurate or not. Hence, the study of laminar-turbulent transition requires more effort.

1.9 Heat Capacity of Molten Alloys

1.9.1 Heat Capacity Background

Heat capacity is used to measure the heat energy required by a system to change temperature. It is related to the size of the system. Specific heat capacity is defined as the heat capacity per mass of pure substance and it can be expressed as per mole or volume, too. The specific heat capacity is of interest for both industrial and academic applications. In industrial areas, precise values for the specific heat capacity of molten metals and alloys are required increasingly for the simulations of numerical analysis. [15]

1.9.2 Heat Capacity Measurement

Thermodynamic calculations of molten metals, such as Gibbs free energy and enthalpy, can be achieved by testing the calorimetric properties of stable undercooled metals. For example, the specific heat and melting enthalpy of undercooled molten metals can be used to predict the glass-forming ability of a certain multicomponent alloys. However, the molten metals and alloys tend to become chemically reactive at high temperature required, which makes measurements of liquid metals/alloys impossible. It causes difficulty for both high temperature experiments like those of molten alloys (e.g. Ti_6Al_4V, 1920K) and those of relatively low temperature alloys with high chemical reactivity. [15] In order to avoid the heterogeneous nucleation and contamination caused by the wall-contact conditions, containerless processing is necessary to accomplish the calorimetric measurements of undercooled molten alloys.

In wall-contact calorimetric devices, the liquid sample has to touch the container so the accuracy of the measured specific heat capacity can be ruined by any reactions. In addition, reactions between the sample and the walls also affect the measurements of other thermophysical properties, like viscosity and surface tension. Various techniques have been investigated to overcome these difficulties.

Electromagnetic levitation (EML) has been applied in the measurements of thermophysical properties of reactive molten alloys [15]. Containerless calorimetry is used in space to accomplish low temperature measurements that cannot be achieved on Earth, like those for glass-forming alloys. In addition, the positioning force required in microgravity to support the sample is so much smaller than on Earth that deformation can be avoided and the molten alloys kept as a sphere during the measurements, privileging the numerical modelling of simple spherical geometry.

Modulated electromagnetic non-contact calorimetry has been used in low temperature physics and adopted by two Spacelab missions. These used the device TEMPUS to accomplish measurements under reduced gravity. [15] The solid sample is positioned by an electromagnetic quadrupole field and heated by a dipole field, which are all generated by the coil system. The temperature on the poles, defined by the symmetric axis of two areas of heating, can be obtained by optical pyrometer and the experiments can be recorded by a high quality camera.

1.9.3 Numerical evaluation of convection in heat capacity measurement

The specific heat capacity of molten melts and alloys can be evaluated from the modulated temperature response. In the thermodynamic calculation, the system should be considered as adiabatic or isothermal to estimate the internal and external heat transport. [15]

For modulation calorimetry, the control voltage of the generator is modulated, and a modulated current is achieved by the computer. The total input power of the heating is composed of two parts. One is generated by the heating field and the other from the position field. According to the experiments, the equator of the sample receives most of the heating powers and the poles get zero. In the work of Wunderlich et al, the sample can be divided to two parts, representing two different thermal conditions. One is heated directly by the heat field, while the other is heated conductively. Figure 1.23 gives a view of the equivalent couple reservoir heat flow model.

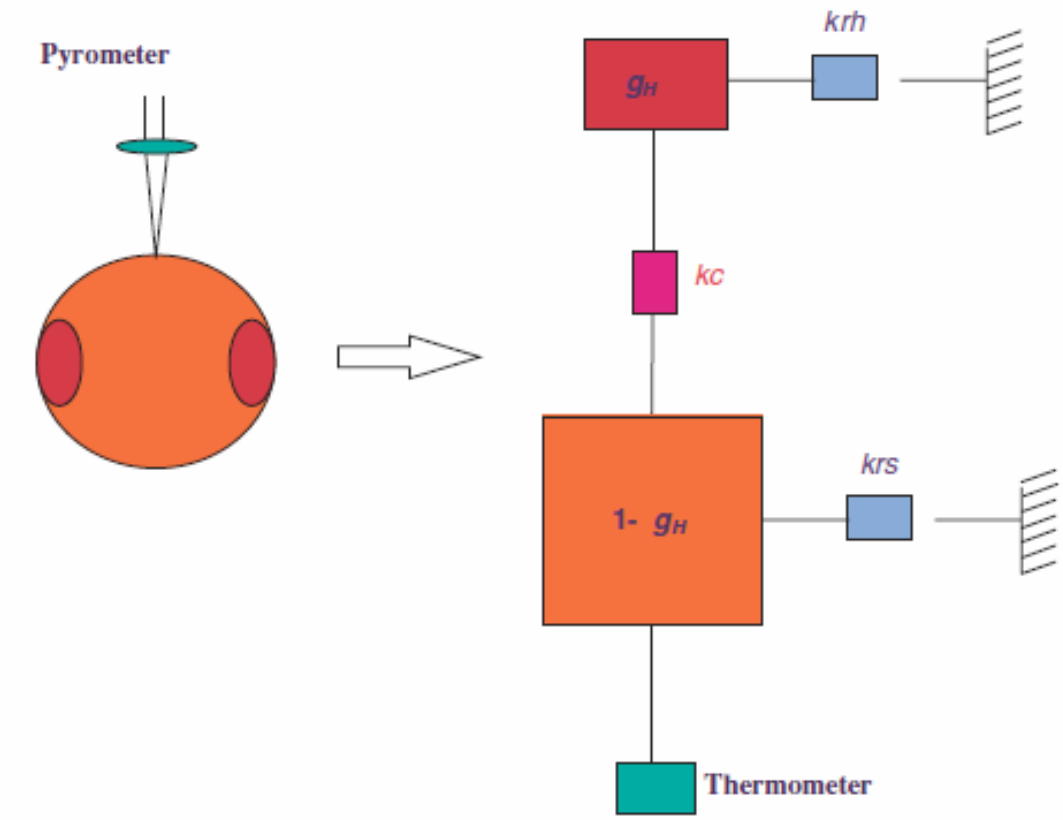

Figure 1.23: Inductively heated sample (Left) and Heat flow model of coupled reservoir (Right). [15]

The heat power is modulated by the computer as a function of time:

$$P_\omega(t) = \Delta P_\omega \cos(\omega t) \tag{1.11}$$

Where $P_\omega(t)$ is heat power input; and t is time.

According to the heat power, a modulated temperature response of half of the amplitude in the amplitude modulation mode can be derived from the heat balance equation:

$$mc_P \frac{dT}{dt} = P_0 + \Delta P_\omega \cos(\omega t) - 4\pi R_0^2 \sigma_{SB} \varepsilon T^4 \tag{1.12}$$

Where c_P is specific Heat; m is sample mass; R_0 is sample radius; ε is hemispherical emissivity; $P_0$is constant power on equilibrium temperature; and σ_{SB} is Stefan-Boltzmann constant.

Since the measurements were completed in an Ultra High Vacuum environment, the only way for the sample to lose heat is radiation, which is expressed by the second term in the equation above.

The figures 1.24 and 1.25 show 2 methods of modulated input heating power corresponding to the temperature response.

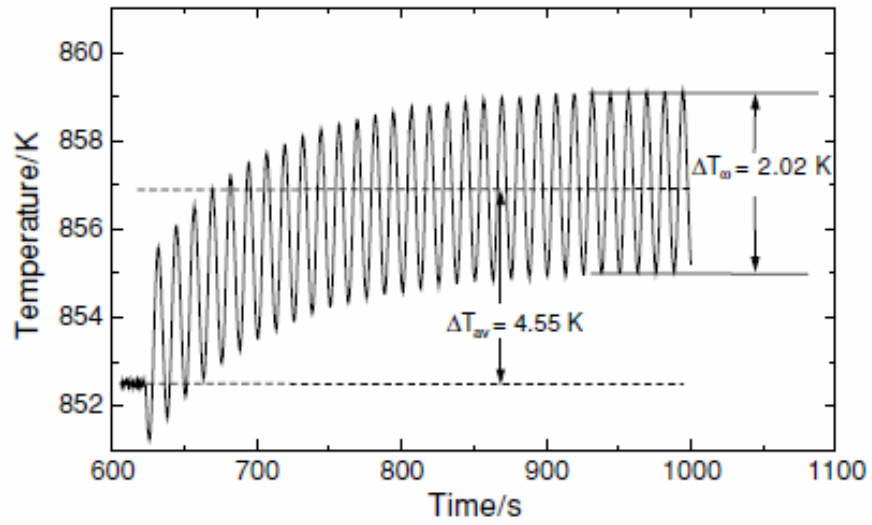

Figure 1.24: Temperature response of the amplitude modulation mode. [15]

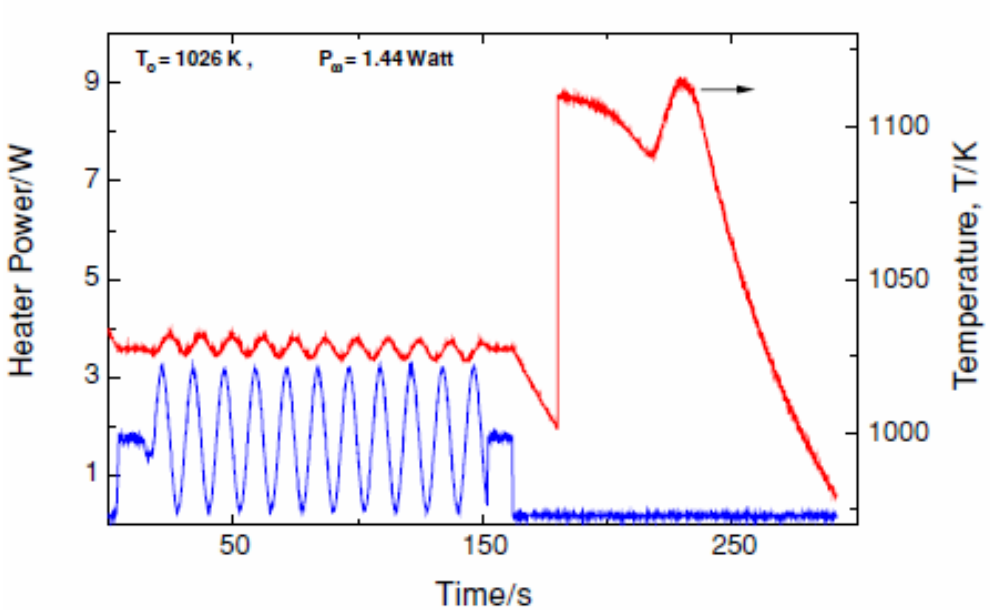

Figure 1.25: Temperature response of the power mode. [15]

The internal temperature gradient is related to the thermal conductivity of the sample. The thermal equilibrium inside the sample can be described by a relaxation time τ_{int}, which means the higher the thermal conductivity, the smaller the relaxation time. The radiation also affects the time required for thermal equilibrium and can be described as relaxation time τ_{ext}. According to the study of Egry *et al.*, when the modulation frequency meets the relation [16]:

$$1/\tau_{ext} \ll \omega \ll 1/\tau_{int} \tag{1.13}$$

The specific heat capacity c_P has a simpler relation with the modulated temperature response ΔT_ω:

$$\Delta T_\omega = \frac{\Delta P_\omega}{\omega c_P} \tag{1.14}$$

Where ΔT_ω is Temperature response; c_P is heat capacity; and ω is frequency.

The heat capacity can be derived from the ΔT_ω, which was obtained from the above methods.

1.9.4 Convection in heat capacity measurement

The internal convection greatly affects the calculation. For example, if the internal convection is turbulent, the high velocity movements of molecules due to the chaos make it easier to achieve thermal equilibrium for the liquid sample. Thus, the sample can be considered as an isothermal system because no temperature gradients exist initially. In other words, the amplitude of the temperature response can be captured more accurately, and used to calculate the specific heat capacity. On the other hand, turbulent internal convection offers a wider range of modulation frequencies from which to choose, which benefits measurements design. Since relaxation time τ_{int} is so small for fast heat transformation, the term $1/\tau_{int}$ turns out to be very large. Thus, the wider range of modulation frequencies provides more choices for scientists to set the experiments. Moreover, if the equation (1.14) is applicable, the accuracy of the calculation will be increased since only temperature response, frequency and heat power input are needed. Therefore, the convection in measurements of specific heat capacity directly relates to the results' accuracy. The internal convection should be under control to sustain turbulence during the measurements.

CHAPTER 2

EXPERIMENT AND ANALYSIS

2.1 Experiment on parabolic flight

A droplet of $NiAl_3$ alloy of 7mm in diameter was electromagnetically levitated and melted on the parabolic flight. SUPOS, an electromagnetic levitation coil set, was adopted for the experiment. The sample was positioned by a quadrupole positioning field operated at 150 kHz and melted by a dipole heating field operated at 356 kHz. Both heating and positioning currents shared the same coil set with different frequencies. The positioning current was kept constant to provide the electromagnetic force to levitate the sample, while the heating current was increased up to a constant value to melt the sample and keep the temperature increasing. The temperature of the sample was measured by optical pyrometry. The motion of tracer particles on the droplet surface gave the time of transition to turbulence of internal convection.

When the sample was fully molten, it could be inferred from the regular and slow motion of particles that the internal flow was laminar (Figure 2.1, Figure 2.2). As the liquid droplet was continuously heated the internal fluid flow accelerated as the temperature kept rising, eventually becoming unstable and then fully turbulence (Figure 2.3). It can be noticed from the video that the motion of tracer particles became chaotic.

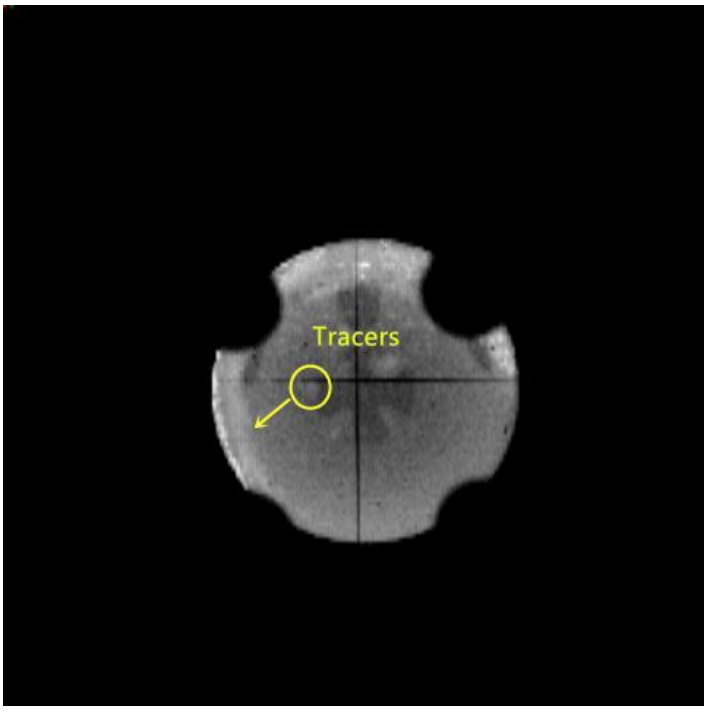

Figure 2.1: Laminar flow—tracer particles (white part in the circle) move out of the pole to accumulate in the band of equator (white band around the sample). The arrow indicates the direction of movements.

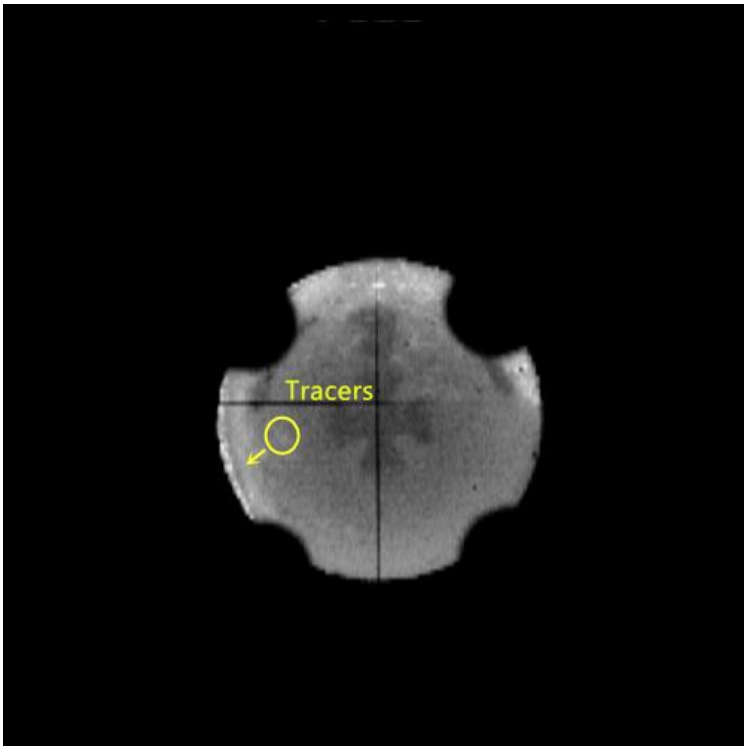

Figure 2.2: Laminar flow—tracer particles (white part in the circle) move closer to the equator.

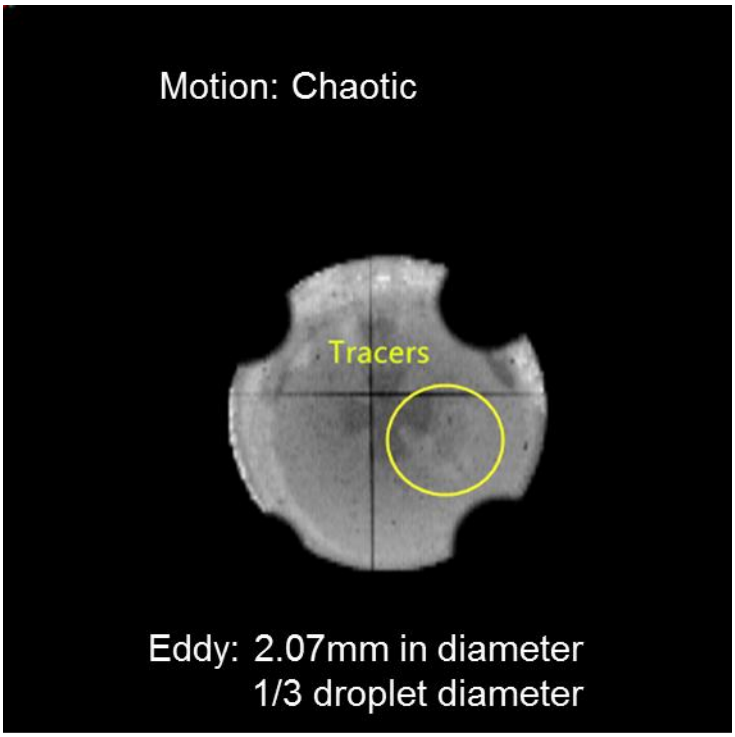

Figure 2.3: Turbulent flow—eddies (white part in the circle, about 2.07mm in diameter)

Although the sample was a sphere of 7mm in diameter at the beginning, the deformation occurred during the melting process. It can be noticed that the sample had become an ellipsoid when the internal convection reached laminar-turbulent transition (Figure 2.4). The radius of the equator kept shrinking as that of the poles enlarged.

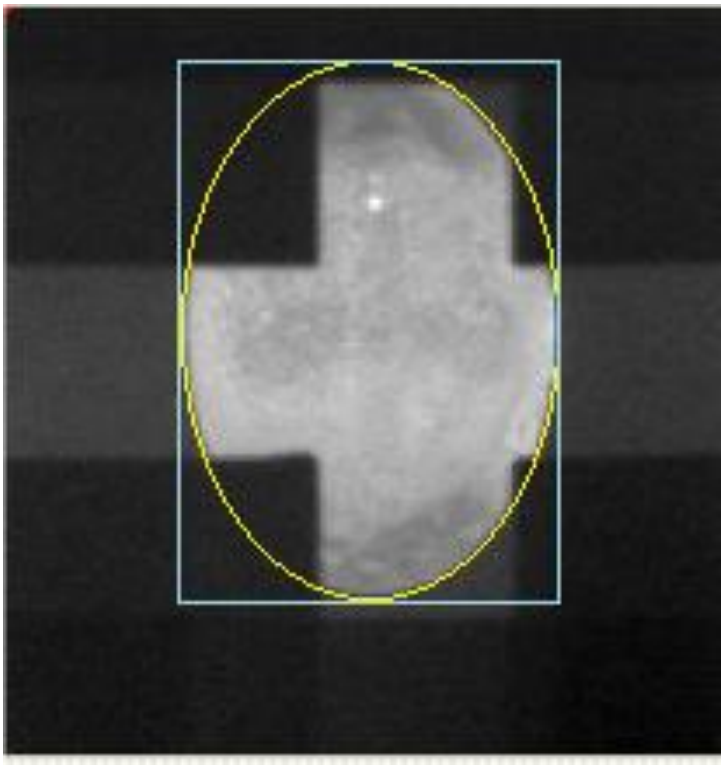

Figure 2.4: Deformed $NiAl_3$ droplet on laminar-turbulent transition.

2.2 Analysis

2.2.1 Force distribution

In EML, the electric current in the coil set is composed of two different frequencies for heating and positioning the samples. The electromagnetic force used to levitate the sample is generated

by the interaction of the induced current and the electromagnetic field, which is called Lorentz force F and can be written as:

$$F = J \times B \tag{2.1}$$

where J is the induced eddy current and B is the magnetic field density [1].

In this EML system, the induced current of the droplet is very responsive to the electromagnetic field generated by coils. Thus it can be considered as a magnetoquasistatic system with reduced Maxwell's equations:

$$\nabla \times \vec{B} = 0 \tag{2.2}$$

$$\nabla \times \vec{E} = -\frac{\partial \vec{B}}{\partial t} \tag{2.3}$$

$$\nabla \times \vec{H} = \vec{J} \tag{2.4}$$

where $\vec{B}$ is the magnetic flux density, $\vec{E}$ is the electric field, $\vec{H}$ is the magnetic field and $\vec{J}$ is the current density.

Since the magnetic Reynolds number is estimated to be small enough that the interaction between the electromagnetic field and the internal convection can be neglected, the calculation of the electromagnetic field can be completed ahead of the fluid flow field. [7]

The mutual inductance method has been applied to solve Maxwell's equations. The sample was assumed to be axisymmetric and discretized. Maxwell's equations were solved based on each mesh to obtain the induced currents in the sample. With the coil currents the density of the magnetic field was calculated. Then the Lorentz force used to levitate the sample was derived. [5] The calculation process was coded [1] and applied as a subroutine to provide the momentum source in the modelling.

The figure 2.5 (Left) shows the force distribution on the sphere sample. Both the magnitude and the direction of the force are expressed by the arrows. It is obvious that the region around the equator of the sample got more electromagnetic force than the poles.

Since the droplet was deformed into an ellipsoid in the experiment, the force distribution changed due to the increased distance between the sample and the coil set. The direction and magnitude of the arrow give the electromagnetic force distribution. It is obvious that the largest force loaded on the sphere geometry was on the equator of the domain while the ellipsoid one received the largest force on the band between the equator and the poles.

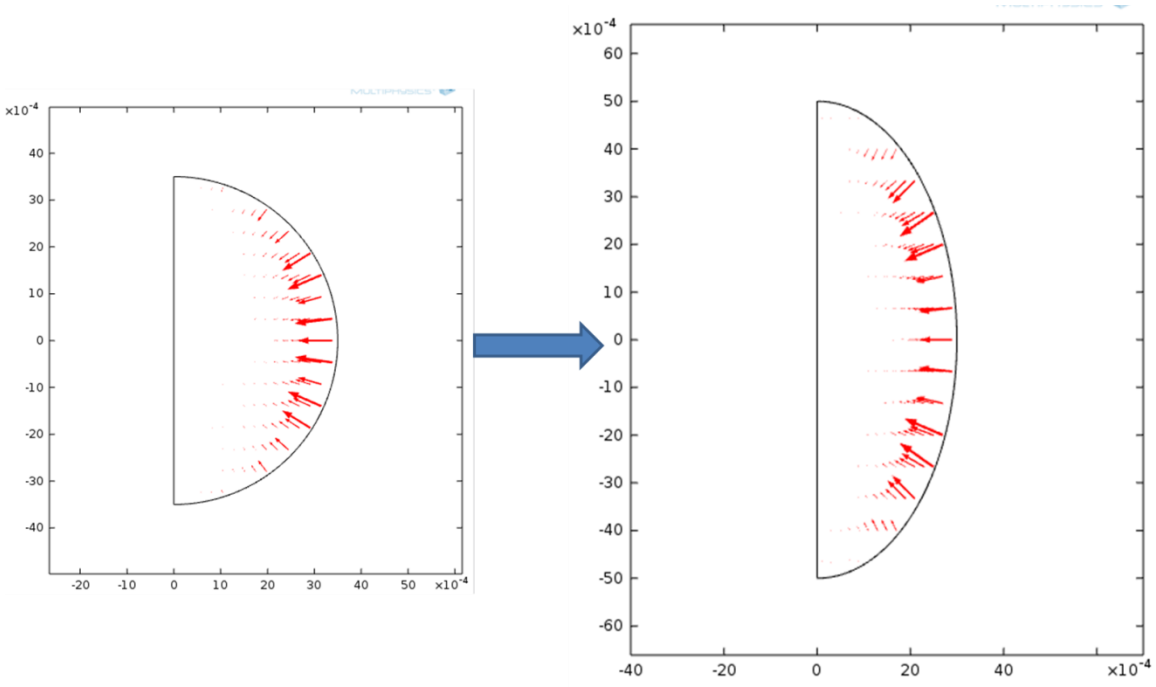

Figure 2.5: The change of electromagnetic force distribution on the sample—from sphere (Left) to ellipsoid (Right).

2.2.2 Turbulent transition phenomena

In the research of Hyers et al. [1], the flow at turbulent transition is regarded as laminar, based on the side view observation of pile of tracer particles on the equator. In this work, the motion of tracer particles can be figured out more clearly from the top view of the sample than from the previously used side view.

The velocity of flow on the droplet surface can be obtained by analyzing the motion of visible particles. By the side view videotape, it can be observed that the small particles on the sample surface flow from the two poles to the equator of the droplet. In the following, as the droplet was heated continuously, the floating particles were accelerated by the internal magnetohydrodynamics (MHD) flow and showed apparent chaotic motion, indicating that the turbulence had begun. However, compared to the record from the side view of the particles' motion, the top view of the droplet pole shows a much more accurate time for the laminar-turbulent transition. From the top view, it can be observed easily that the particles drawn by the internal laminar flow move out from the pole and travel to collect on the equator directly, indicating the formation of corotating toroidal loops inside the droplet. When the direction of the particles changed—inward toward the poles—that implies the inner flow became chaotic, and laminar-turbulent transition started. Meanwhile, the change of the stagnation line is too slight to be noticed from the side view. In other words, because the stagnation line would remain stable in the turbulent transition, the method of using the stagnation line to indicate the internal convection state is not accurate. Another few seconds are needed for the stagnation line to show the instability and break. Since the sample was heated continuously, the temperature captured by the side view when the stagnation line broke was higher than for turbulent transition.

In this work, the thermophysical properties like density, electrical conductivity, and viscosity are related to the sample temperature directly. The change to top view observation can provide a

more precise value for the thermophysical properties in order to obtain a more accurate evaluation of internal convection in EML droplet by numerical modelling.

2.2.3 Convection in $NiAl_3$ sample

The current in this set of coils is superposed，which means there is only one set of coil which provides both the positioning field (quadrupole) and the heating field (dipole) at the same time. Both the heating and positioning fields drive convections in the droplet.

The internal convection is governed by the Navier-Stokes equations (1.1) and (1.2) with boundary conditions in equations (1.7) and (1.8).

Following the method of Hyers, et al. [2], the flow was simulated in a NiAl3 sample at the temperature of laminar-turbulent transition, 1472.15K, in MSL-EML. The experiment parameters are: Positioning control Voltage=10V and Heating control Voltage=10V.

CHAPTER 3

EXPERIMENT RECORD

The convection in the liquid sample was evaluated by the motion of tracer particles which were driven by the internal flow. The tracers were floating on the surface of the sample during the experiment. The velocity of internal fluid flow close to the sample surface can be obtained by analyzing the pattern of tracer particles.

3.1 The velocity captured from a tracer particle.

Based on the analysis of the experiment, the top view observation gave a more accurate moment for the laminar-turbulent transition. To calculate the velocity of tracer particles just before the laminar-turbulent transition, single particle has been picked for its clear motion from the top view video tape. The figure 3.1 were captured to show the movement of the tracer, which moved from the pole to the band near the equator.

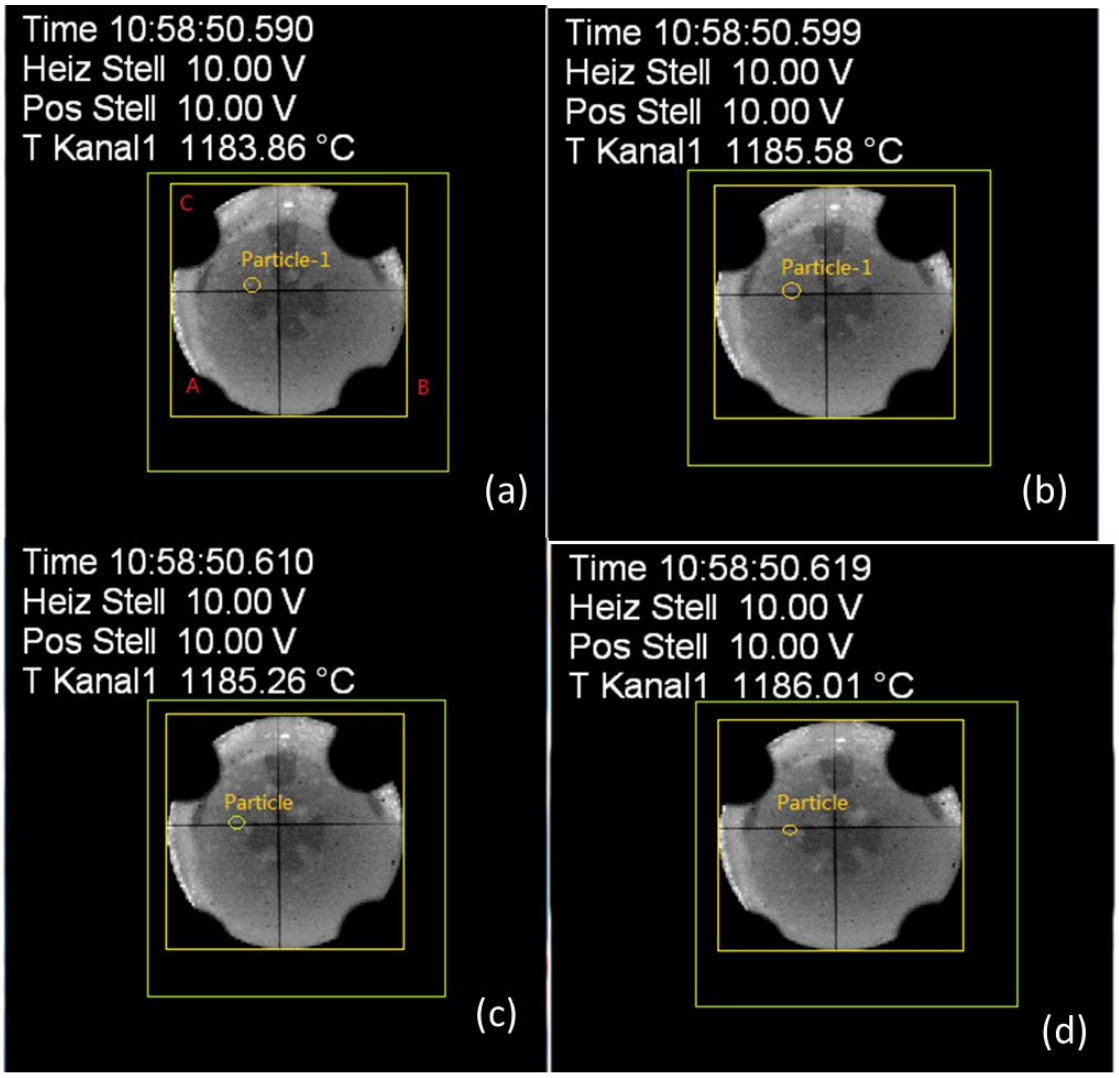
Time 10:58:50.590
Heiz Stell 10.00 V
Pos Stell 10.00 V
T Kanal1 1183.86 °C
C
Particle-1
A
B
(a)
Time 10:58:50.599
Heiz Stell 10.00 V
Pos Stell 10.00 V
T Kanal1 1185.58 °C
Particle-1
(b)
Time 10:58:50.610
Heiz Stell 10.00 V
Pos Stell 10.00 V
T Kanal1 1185.26 °C
Particle
(c)
Time 10:58:50.619
Heiz Stell 10.00 V
Pos Stell 10.00 V
T Kanal1 1186.01 °C
Particle
(d)

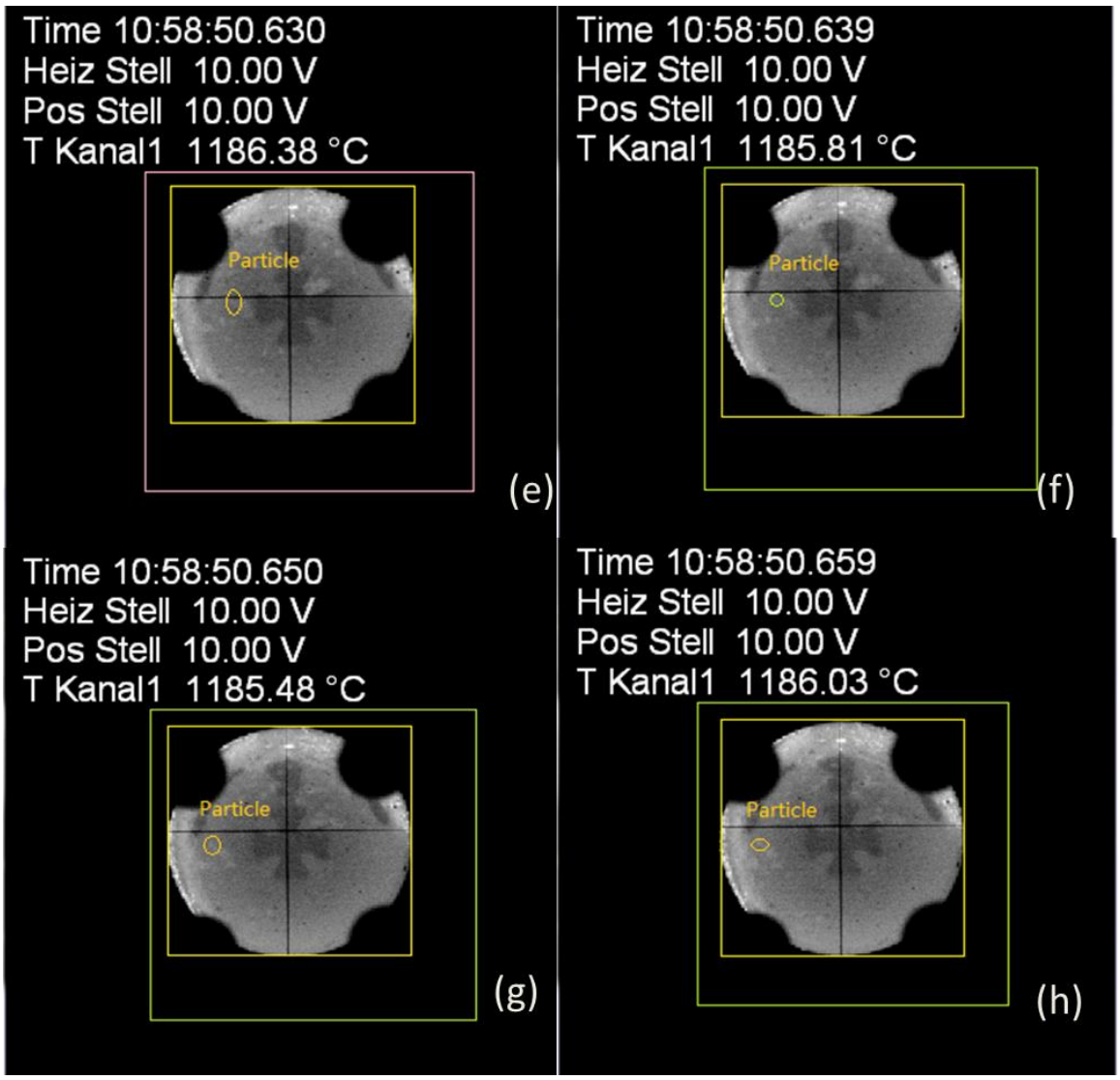
Time 10:58:50.630
Heiz Stell 10.00 V
Pos Stell 10.00 V
T Kanal1 1186.38 °C
Particle
(e)
Time 10:58:50.639
Heiz Stell 10.00 V
Pos Stell 10.00 V
T Kanal1 1185.81 °C
Particle
(f)
Time 10:58:50.650
Heiz Stell 10.00 V
Pos Stell 10.00 V
T Kanal1 1185.48 °C
Particle
(g)
Time 10:58:50.659
Heiz Stell 10.00 V
Pos Stell 10.00 V
T Kanal1 1186.03 °C
Particle
(h)

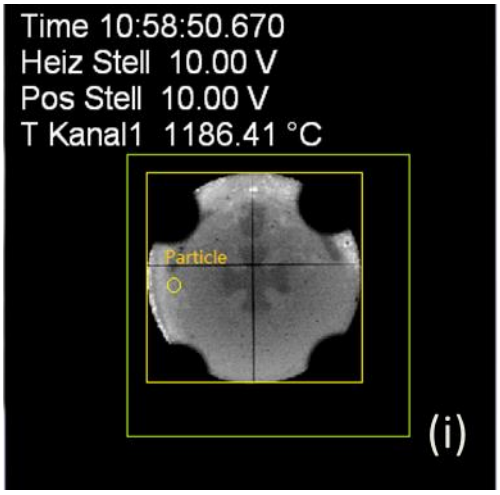

Figure 3.1: The path of the picked tracer particle moving on the sample surface drawn by the internal convection—from the pole to the band directly.

The length of the tracer's path was obtained from the shape of the deformed droplet, which is an ellipsoid recorded by the side view observation. The figure 3.2 is the deformed droplet.

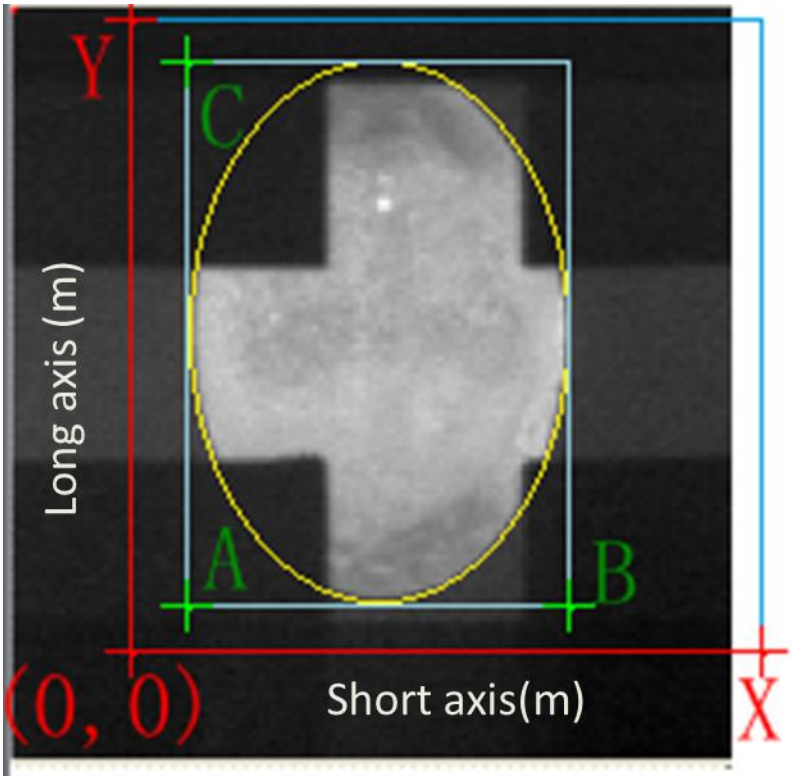

Figure 3.2: Deformed droplet on laminar-turbulent transition.

The size of the deformed droplet was captured manually, using the description of the ellipsoid provided by the equation 3.1:

$$\frac{x^2}{a^2}+\frac{y^2}{b^2}=1 \qquad (3.1)$$

Where a is 3.12 mm and b is 4.42 mm. That means that on the laminar-turbulent transition, the sphere sample had become an ellipsoid with semi-minor axis of 3.12 mm on the horizontal plane and semi-major axis of 4.42 mm vertically. The path of the tracer was illustrated in the figure 3.3:

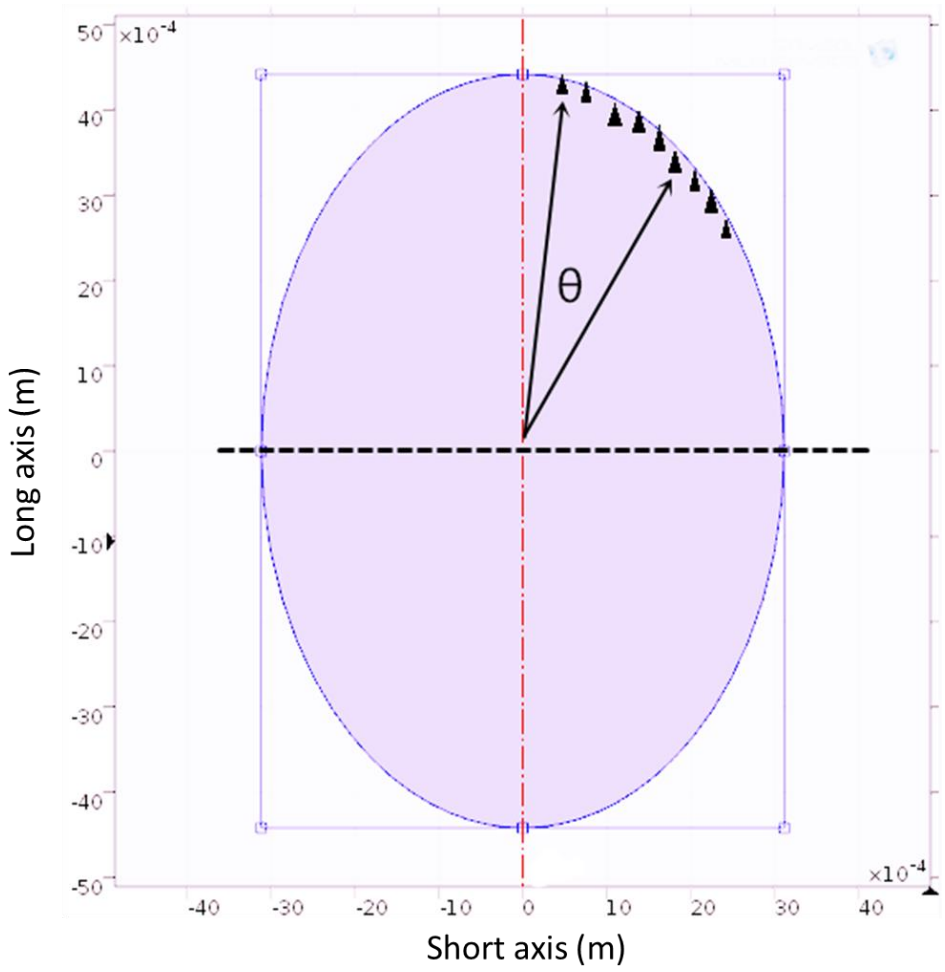

Figure 3.3: The points picked on in modelling for showing the path of the tracer particle.

The arc length between two points was estimated by the following equations. The initial value of θ was 0, meaning the arc length between the point and the pole was derived.

$$L = \int_0^{2\alpha} \sqrt{(b^2 + a^2) - (b^2 - a^2)\cos\theta}\, d\theta \tag{3.2}$$

Where L is the length and α is the angle between the selected point and the pole, estimated by the equation:

$$\alpha = \cos^{-1}\frac{y}{b} \tag{3.3}$$

Thus, the displacement of the particle moving from the pole can be calculated by the equation (3.2) and (3.3).

The table 3.1 gives the calculation:

Table 3.1: Displacement of the picked tracer particle—L (arc length).

NO.	Time (s)	Δt (mm)	x (mm)	y (mm)	y/b	2α	L (mm)
1	50.59		1.137	4.112	0.931	0.747	3.366
2	50.599	0.009	1.189	4.083	0.924	0.783	3.534
3	50.61	0.011	1.294	4.018	0.910	0.856	3.883
4	50.619	0.009	1.308	4.009	0.908	0.866	3.930
5	50.63	0.011	1.485	3.883	0.879	0.994	4.545
6	50.639	0.009	1.704	3.698	0.837	1.157	5.356
7	50.65	0.011	2.042	3.336	0.755	1.429	6.758
8	50.659	0.009	2.147	3.201	0.725	1.521	7.244
9	50.67	0.011	2.432	2.762	0.625	1.791	8.725

The figure 3.4 show the displacement of the point away from the pole.

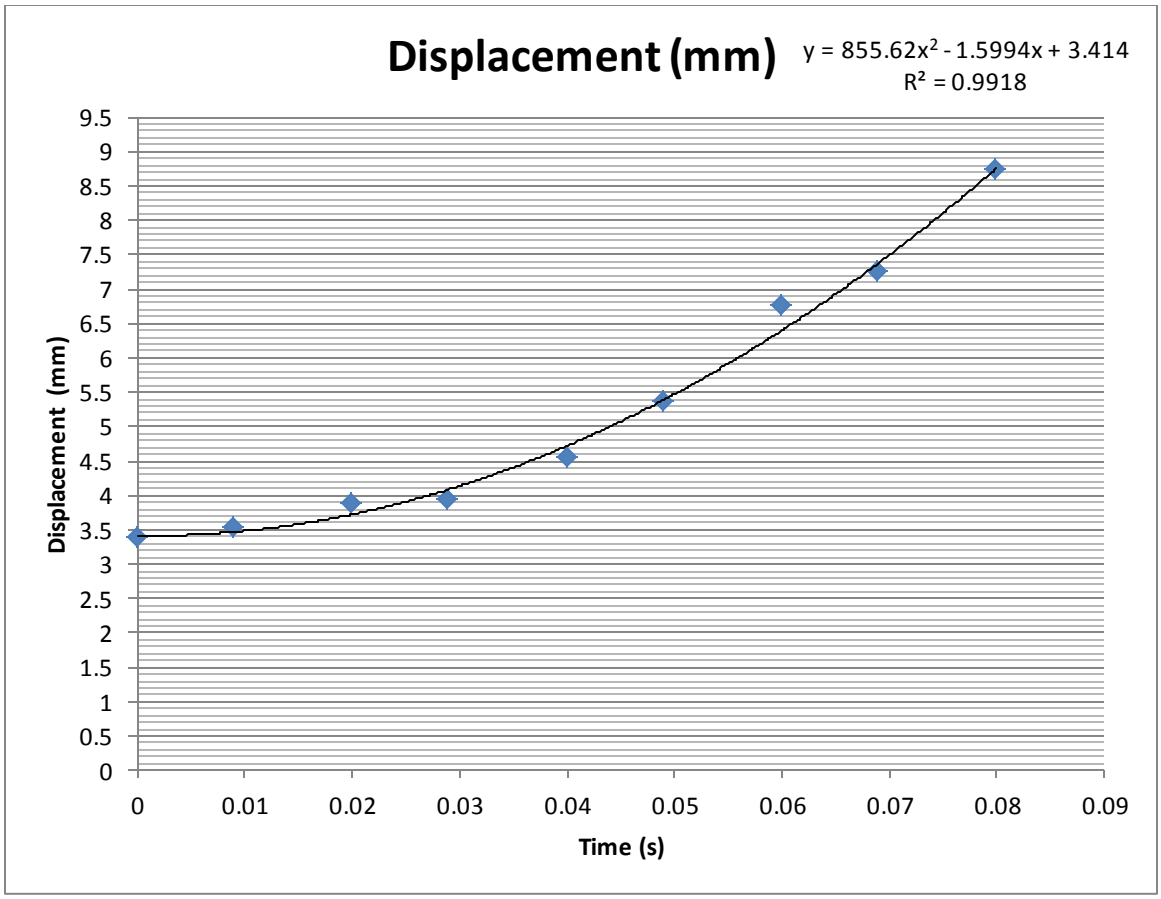

Figure 3.4: The displacement of the tracer particles vs. time.

From the figure 3.4, it was obvious that the data can be fitted well by the equation:

$$s = 855.62t^2 - 1.5994t + 3.414 \qquad (3.4)$$

where s is the travelling displacement of the tracer particle away from the pole, which was the arc length L calculated by the equation (8.2) and (8.3).

The average velocity of the tracer was v=76.4 mm/s. Thus, the Reynolds number just before the laminar-turbulent transition was derived by the equation (Equation 1.8) and turns out to be 860. Furthermore, the acceleration of the tracer particle turned out to be a constant. The relative error increased as the particle moved toward the equation because of the smaller projection of each increment of arc length.

From Hyers' previous work, the laminar-turbulent transition was regarded as steady state and the Reynolds number at the turbulent transition was evaluated to be 600, which is close to the one estimated by this work.

3.2 Stokes number of the tracer particle

Although the velocity of the tracer particle floating on the surface of the sample has been calculated already, that cannot be regarded as the convection velocity. Since the particle was drawn by the fluid flow, it may have moved slower than the internal fluid.

The tracer particles which were drawn out of the poles by fluid flow are composed of certain Ni-Al alloy. From the phase diagram (Figure 4.1), the composition may have more Ni, for the particles were the last to melt and the first to freeze.

The Stokes number of the tracer particle can be derived from the following equation:

$$\mathrm{Stk} = \frac{\tau_p u}{D} \tag{3.5}$$

where u is the velocity of the convection and D represent the diameter of the sample. τ_p is the relaxation time of the particle.

Assuming the difference in particle and fluid velocity is small (Re<1), the τ can be expressed as:

$$\tau = \frac{\Delta\rho d_p^2}{18\mu} \tag{3.6}$$

Where $\Delta\rho$ is the density difference between the tracer particles and the fluid; μ is the fluid viscosity and d_p is the diameter of the tracer particle.

The tracer particles left floating on the sample surface were the remainder after the melting process and it was not easy to figure the exact material out. Thus, the extreme condition would be assumed that the tracer particles were all made of Ni with the density of ρ_p=7900 Kg/m^3 and the density difference was calculated as $\Delta\rho=\rho_p-\rho$=3181.81 Kg/m^3.

The calculation of the Stokes number was completed with the table of the convection and tracers' properties (Table 3.2).

Table 3.2: Calculation for the Stokes number.

Properties	ρ_p Kg/m^3	ρ Kg/m^3	$\Delta\rho$ Kg/m^3	d_p m	μ Pa*s
Value	7900	4718.92	3181.08	0.00029	0.0029
Properties	τ_p s	u m/s	D m	Stokes number	
Value	0.0051	0.076	0.07	0.0056	

The Stokes number 0.0056 turned out to be much less than 1, which means the assumption matched the experiment. The relative velocity between the tracer particles and the internal convection can be neglected that the tracer particles' movement on the sample surface show the convection conditions.

The steady solid band covering the equator may possibly be Al_2O_3, which was expected to vaporize and stick to experiment facilities during the experiments, such as the coil set.

CHAPTER 4

NUMERICAL EVALUATION

4.1 Thermophysical properties

The thermophysical properties of the sample, $NiAl_3$, needed by modelling can be determined in turn. The study of Egry *et al.* [18] provided the equations 4.1 and 4.2 with the table 4.1 and 4.2 to fit the electrical conductivity and viscosity.

Electrical conductivity:

$$\sigma(\mathrm{T}) = \sigma(T_L) + m_\sigma(T - T_L) \tag{4.1}$$

Table 4.1 Electrical conductivity

C_{AL} [at%]	T_L [K]	$\sigma(T_L)$ [$\Omega^{-1}m^{-1}$]	m_σ [$\Omega^{-1}m^{-1}K^{-1}$]	T [K]
75	1398	1016500	59	1472.15

Viscosity:

$$\eta(\mathrm{T}) = \eta_0 + m_\eta T \tag{4.2}$$

Table 4.2 Viscosity

C_{AL} [at%]	η_0 [mPa*s]	m_η [(mPa*s)/K]	T [K]
75	7.94	-0.0034	1472.15

The temperature captured from the top view of the video at the laminar-turbulent transition is 1472.15K. Given the composition of the sample, the electrical conductivity and viscosity at laminar-turbulent transition can be derived to 1.02E+6 Ω-1m-1 and 2.93 mPa*s.

The melting point of the NiAl3 was necessary for the calculation of density and it could be derived from the phase diagram of a Ni-Al alloy system (Figure 4.1). [17]

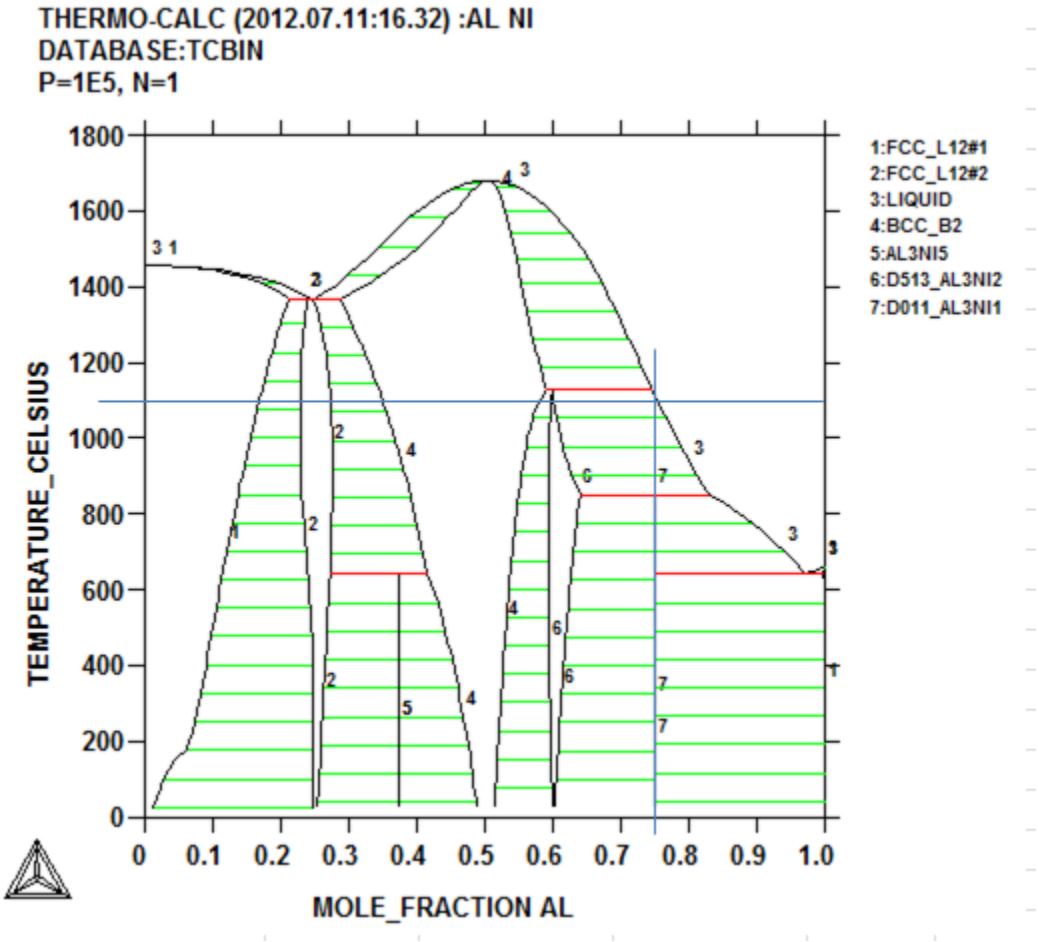

Figure 4.1: phase diagram of a Ni-Al alloy system

According to the mole fraction of NiAl3, the melting point of the alloy turns out to be 1100℃, 1373.15K. Thus, the density of the alloy at the laminar-turbulent transition can be derived from the following equation with the data of metal densities [17]:

$$\rho = \rho_m + k(T - T_{melting}) \quad (4.3)$$

where ρ is Density at a certain temperature; ρ_m is density at the melting point; k is temperature dependence of density and T_m is temperature at the melting point.

Table 4.3: Metal thermophysical properties [17]

	Molecular Weight	Melting Point (K)	at%	wt%	k (kg/m^3K)
Ni	58.69	1728.15	0.25	0.42	-1.19
Al	26.98	933.47	0.75	0.58	-0.35
NiAl3		1373.15			-0.7

Table 4.4: Alloy density

Density (Kg/m^3)	Melting point of Metals	Melting point of Alloy (1373.15K)	Transition Temperature (1472.15K)
Ni	7900	8322.45	
Al	2380	2226.11	
$NiAl_3$		4788.52	4718.92

The density of the $NiAl_3$ was estimated to be 4718.92 kg/m^3 based on the density of Ni and Al. The following table shows the material properties adopted in current models.

Table 4.5 Thermophysical properties

Material Properties	$NiAl_3$	Error
Electrical conductivity ($\Omega^{-1}m^{-1}$) [18]	1.02E+06	
Viscosity (mPa*s) [18]	2.93	25%
Density (Kg/m^3) [17]	4718.92	1%

4.2 Research method

4.2.1 Background

The fluid flow in the EML droplet has been simulated with magnetohydrodynamic models based on clearly visible tracer patterns to calculate the Reynolds number at laminar-turbulent transition.

In Hyers' previous work [1], the internal convection of EML droplets at laminar-turbulent transition in microgravity was regarded as laminar in steady state and was numerically evaluated. Also in that work, the geometry of a droplet was defined as a sphere since the force required in microgravity to levitate a droplet in space was small enough that the sample could keep its shape during the experiments. The simulation result of the steady state model gave the internal convection pattern with two recirculation loops. (Figure 2.2) The predicted Reynolds number at turbulent transition should be derived from the maximum value of velocity; simulation places this number around 600.

4.2.2 Magnetohydrodynamics (MHD) models

In this work, a 2-D steady-state model adopting the commercial software COMSOL was applied at first. However, it failed to work. Many initial conditions of velocity and mesh arrangements have been taken into account, but the numerical calculation still do not converge.

Another two steady-state models using both COMSOL and ANSYS have been applied, in which the internal convection was regarded as turbulent instead of laminar. The calculation of the COMSOL model was considered to be diverged again due to the unreasonable turbulence viscosity evaluation. The model using ANSYS performed well and gave a convergent calculation. The time-averaged velocity field obtained from the turbulence model is very similar to the laminar ones gotten by the Hyers et al. study, which has two symmetric loops directed inward on the equator. However, the maximum velocity calculated is so large that the Reynolds number has reached up to more than 9000, which is too large to be considered laminar flow. The Reynolds number for laminar flow in a pipe should be less than 2000 and convection with Reynolds number larger than 4000 is regarded as turbulence. While in an EML droplet, the Reynolds numbers at the laminar-turbulent transition was around 600. [1] Since the shape of the sample was between that of a sphere and a pipe, the Reynolds number could be believed between 600 and 2000. It can be concluded that the convection in that situation (Positioning control Voltage=10V, Heating control Voltage=10V, Temperature=1472.15K) would become a turbulent in the end.

Therefore, new transient models were developed in which the process of laminar-turbulent transition is traced as a function of time. The period required by the internal flow to transfer to turbulence is going to be captured to compare with that from experiments. The evolution of the velocity field can be analyzed frame-by-frame corresponding to the value of maximum velocity.

Since the calculation from the transient models did not match the time to transition obtained from the experiment, the different boundary conditions were taken into account. According to the

experiment record, there was a wide band which was whiter than other area around the poles. In the simulation, the band was considered as solid, instead of liquid, floating on the liquid sample surface. The range of the solid was captured manually from the experiment record so that the boundary condition was defined as "slip" (liquid) and "no slip" (solid band). However, the time to transition obtained by simulation turned out to be around 0.003s, which failed to match with the experiment either.

The internal condition of the liquid sample was taken into account too. The existence of the solid tracer particles indicates there was solid inside. Since the sample deformed to a smooth ellipsoid, it was impossible that a large amount of the solid left in the sample. To figure out the effect of the solid on flow, the sample was assumed to have a large amount of solid portion in the center which was of shape of apple core. The boundary conditions were applied, too. The models still provided a time to transition of 0.003s, which failed to match with that of experiment.

4.2.3 Geometry

In the simulations completed by Hyers et al. [1], it is reasonable to consider the droplet as a sphere at the laminar-turbulent transition since the positioning force needed in space is small enough to neglect its effect on the sample shape. While in this work, a droplet of NiAl3 was electromagnetically levitated in parabolic flight experiments. The force distribution on the sample is different from that in microgravity experiments. To guarantee the safety of the experiments, it is necessary for the sample to sustain an equilibrium position in the holder, or at least not escape from the holder. Thus, the force provided by the positioning field is much larger than that required by levitation.

From the record of the side view, it's easy to notice that the shape of the sample began to deform even before the sample totally melted. The radius of the equator kept shrinking as that of the

poles enlarged during the melting process. The droplet had become an ellipsoid at the laminar-turbulent transition. Therefore, in this work both sphere and ellipsoid geometry should be taken into account and the ellipsoid mesh is expected to give a much more accurate result than a sphere one.

Two 2-D axi-symmetric geometries have been adopted by the numerical modeling of EML NiAl3 droplet. Figure 4.2 shows the two different geometries applied by the simulation. The left one is an ideal sphere, as in previous simulations, which assumes the droplet retained its shape over the experiment (Figure 4.2 Left). The right one is an ellipsoid, which was captured from frames of side view record (Figure 4.1). Here, the droplet was deformed on the laminar-turbulent transition. (Figure 4.2 Right)

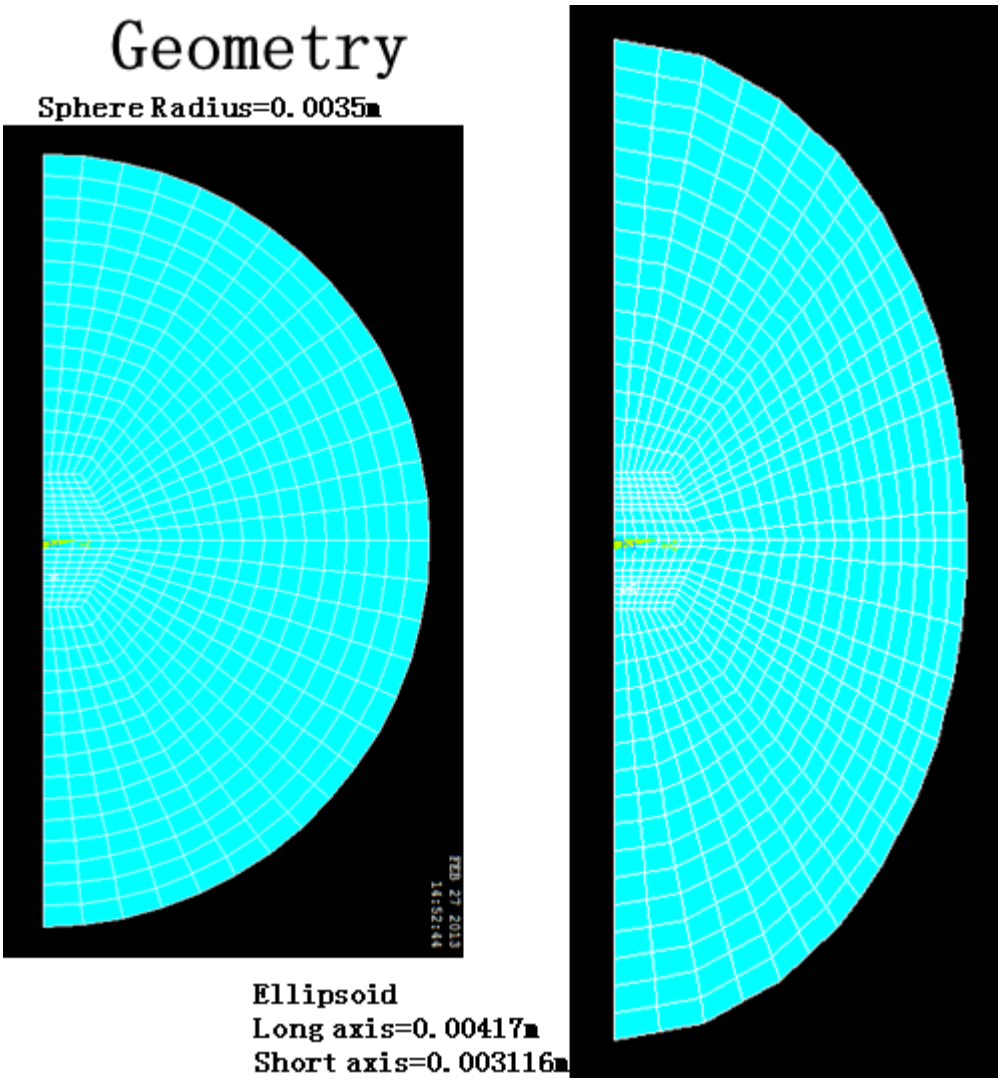

Figure 4.2: Mesh. Left: Sphere, 7mm in diameter; Right: Ellipsoid, 8.82mm in long axis and 6.22 in short axis.

4.2.4 Boundary conditions

In all the steady state models and the first few transient models, the droplet was supposed to hold free surface—"Slip" (Figure 4.3), which means both the normal component of velocity and shear stress on the surface are equal to zero, because the sample was believed to have been fully molten

when the laminar-turbulent transition occurred. The equations for free surface of laminar flow refer to equation (1.6).

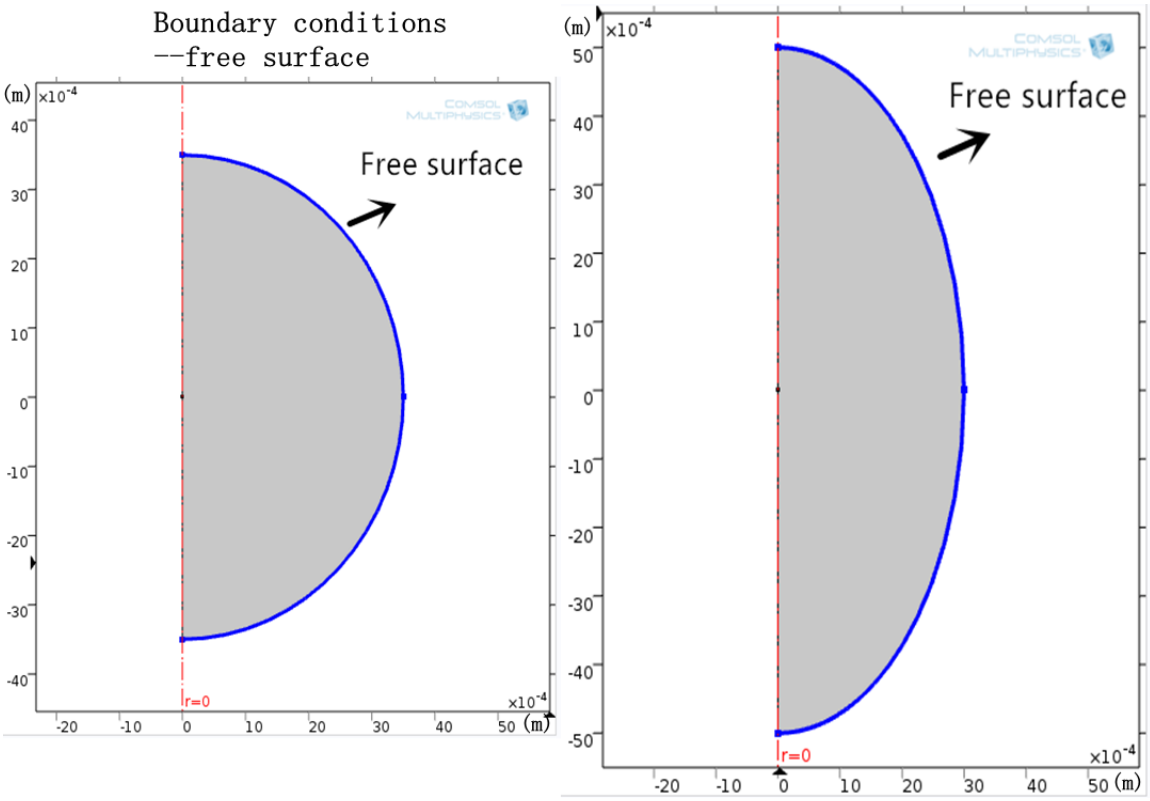

Figure 4.3 : The boundary condition was defined as free surface—"Slip". The left one adopted the geometry of sphere and the right one used ellipsoid.

Since all the models are all 2-D axis-symmetrical, the condition on the axis was pretty similar to the surface (Figure 4.4) —both the normal component of velocity on the axis and the derivative of velocity perpendicular to the axis are equal to zero (Equation 4.4 and 4.5):

$$\left.\frac{\partial \mu_z}{\partial r_{cyl}}\right|_{r_{cyl}} = 0 \tag{4.4}$$

$$\mathrm{u} \cdot i_{r_{cyl}}\Big|_{r_{cyl}} = 0 \tag{4.5}$$

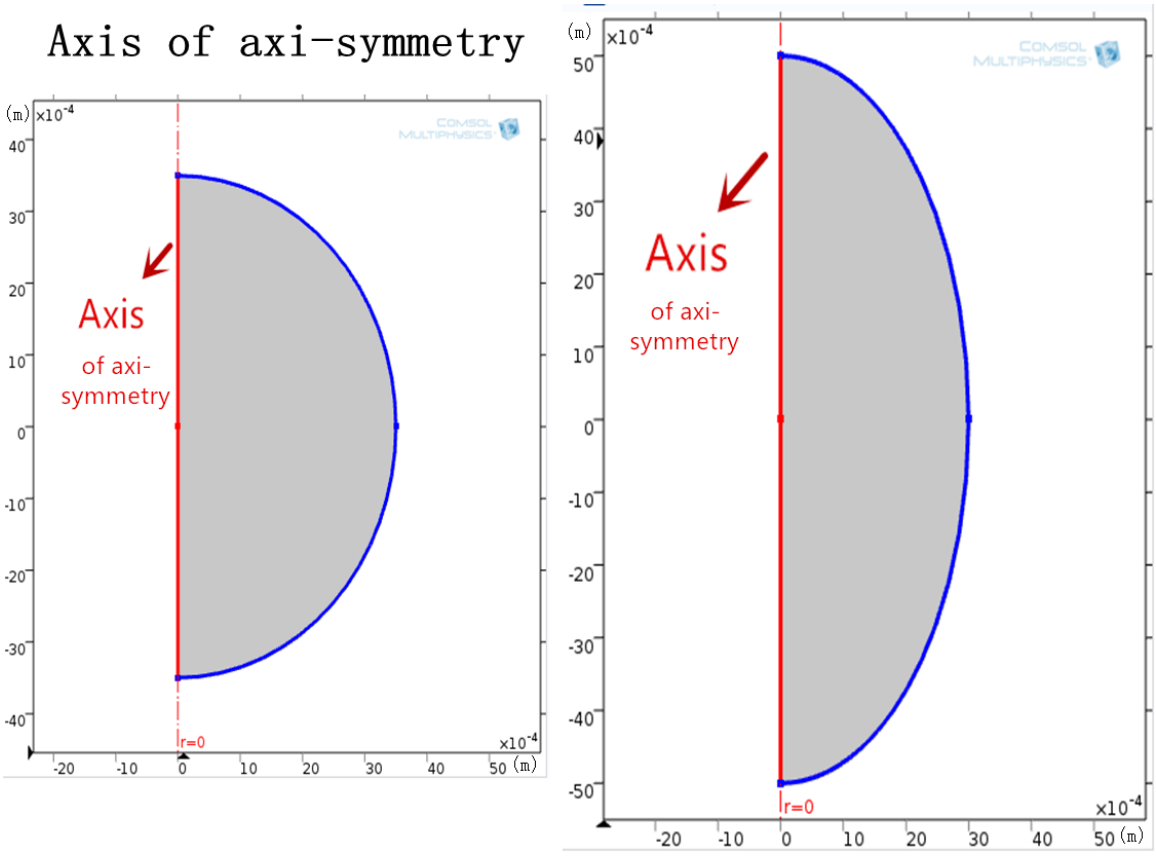

Figure 4.4: Symmetric axis in both sphere (Left) and ellipsoid (Right) geometry.

From the experiment record, the tracer particles accumulated to give a band around the equator of the sample, which was the brighter part observed by the side view (Figure 4.5 Left). This collection of the tracer particles was regarded as a solid, meaning for certain models, the boundary conditions were made up of combined "Slip+non-Slip" surfaces.

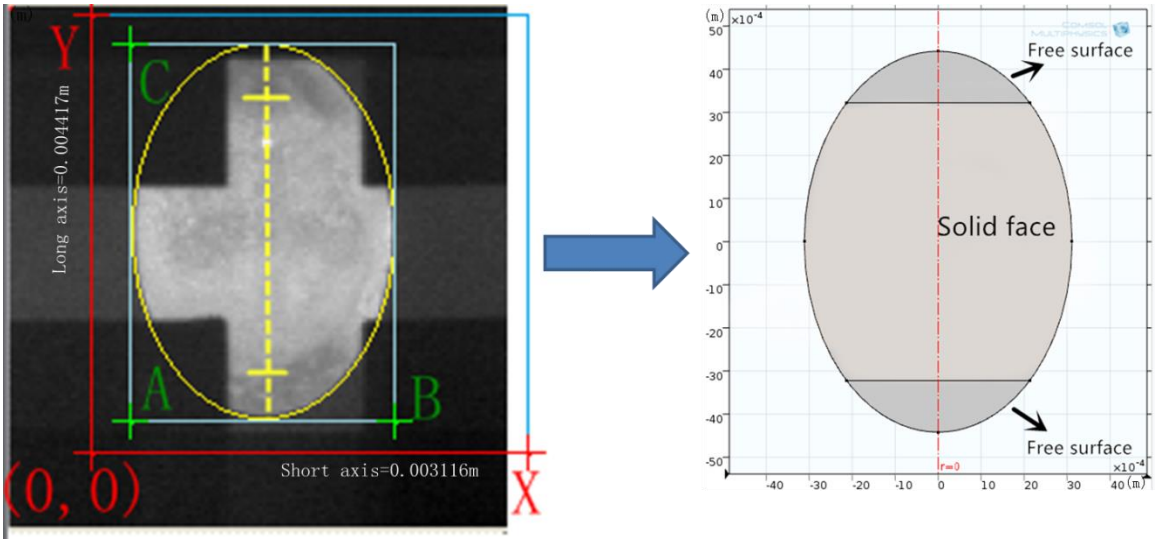

Figure 4.5: The band (Brighter area in the left picture) on the equator was composed of unsolved tracer particles, which created a solid shell impeded the internal fluid flow (Right).

In modelling, the boundary conditions were defined just like the figure 4.6.

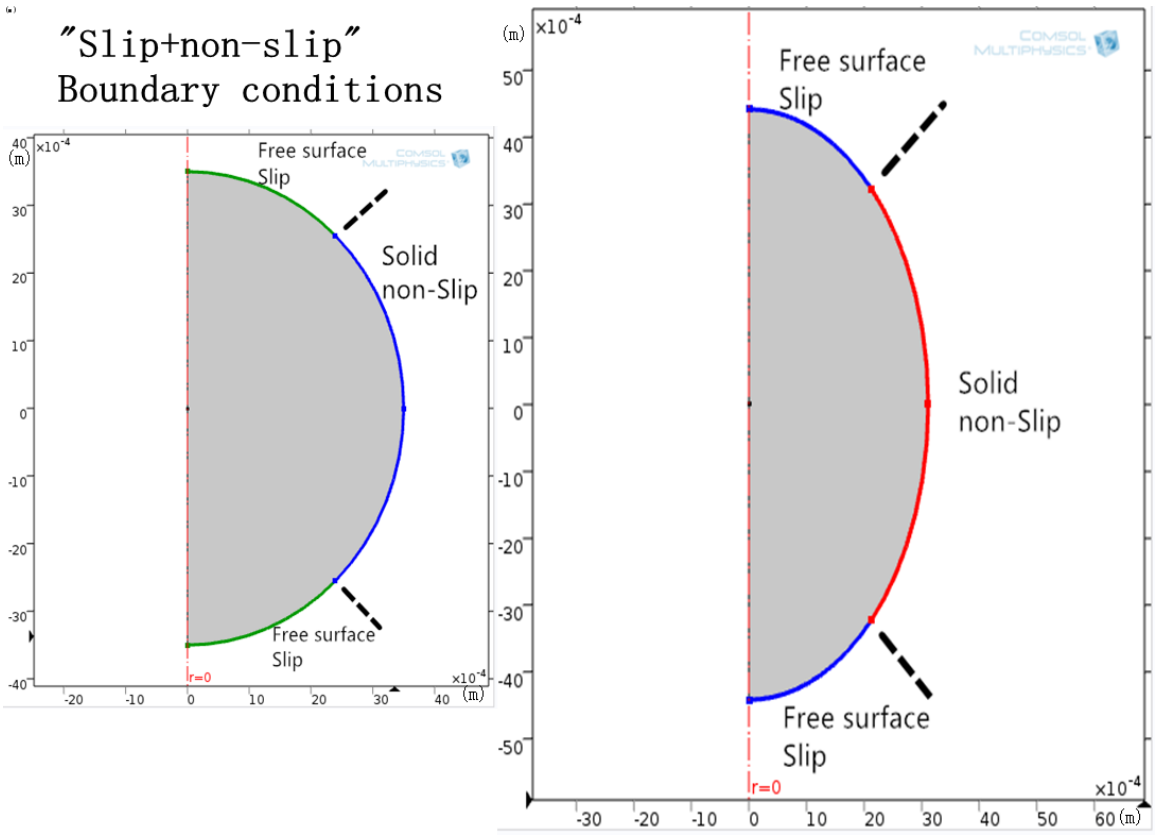

Figure 4.6: "Slip+non-Slip" boundary conditions on both sphere and ellipsoid geometry.

4.2.5 Solid core

Since neither the geometry nor boundary conditions matters the time to transition, a model with a solid core was made to see whether the internal condition affects the simulation result. The "solid core" means that the sample was considered as part molten when the laminar-turbulent transition occurred and the core area of the sample was defined as solid like an apple core. Because the area of the equator received more heating energy with a higher temperature and the direction of the flow was inward on the equator. Both of those factors were good for the melting process. Thus, the shape of the solid core was defined as the figure 4.7.

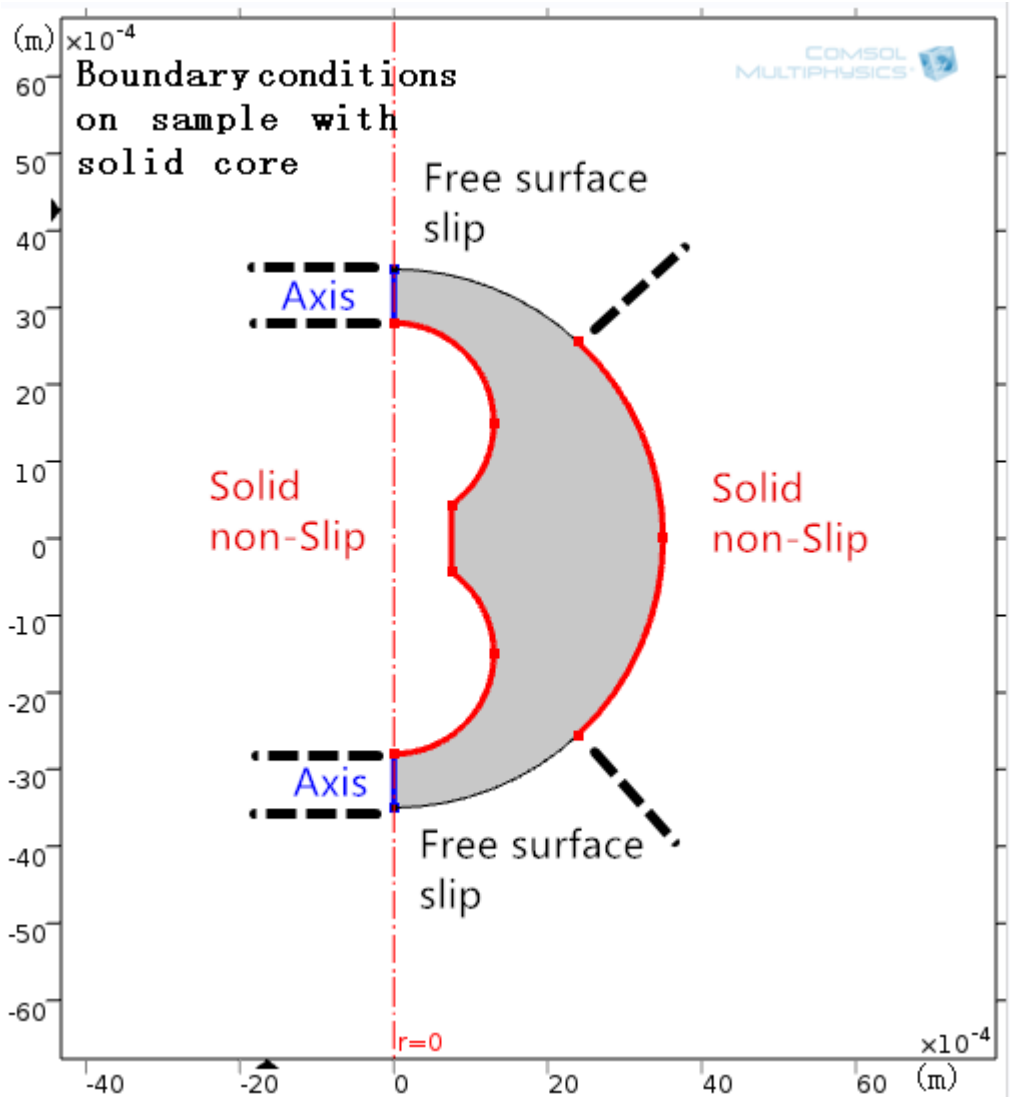

Figure 4.7: The boundary conditions in the model with a solid core, which are assumed to have a non-slip boundary condition at the interface between the solid core and the liquid part.

4.2.6 Summary

Table 4.6 gives a brief summary of the models that have been tested. The calculation for the first 2 groups did not converge, so the internal convection was not in a steady state. The 3rd steady state model provided a converged calculation, but the convection was considered turbulent flow

instead of high-Reynolds-number laminar. Thus, the fluid flow should become turbulent eventually. The 4th, 5th, and 6th groups adopted the transient model in which convection was not independent of time and the time to transition obtained from the models would be compared with the one acquired from the experiment record. The geometry, boundary conditions, and the internal structure were also listed in the table.

Table 4.6 Numerical Models

	State	Convection	Mesh	Boundary Conditions	Internal condition	Commercial Software	Calculation
1	Steady State	Laminar	Sphere	Slip	Liquid	COMSOL	Did Not Converge
2	Steady State	Turbulent	Sphere	Slip	Liquid	COMSOL	Did Not Converge
3	Steady State	Turbulent	Sphere & Ellipsoid	Slip	Liquid	ANSYS	Converged
4	Transient	Laminar	Sphere & Ellipsoid	Slip	Liquid	COMSOL	Converged
5	Transient	Laminar	Sphere & Ellipsoid	Slip & Slip+non-Slip	Liquid	COMSOL	Converged
6	Transient	Laminar	Sphere & Ellipsoid	Slip & Slip+non-Slip	Solid core	COMSOL	Converged

CHAPTER 5

SIMULATION RESULT

5.1 Steady state model

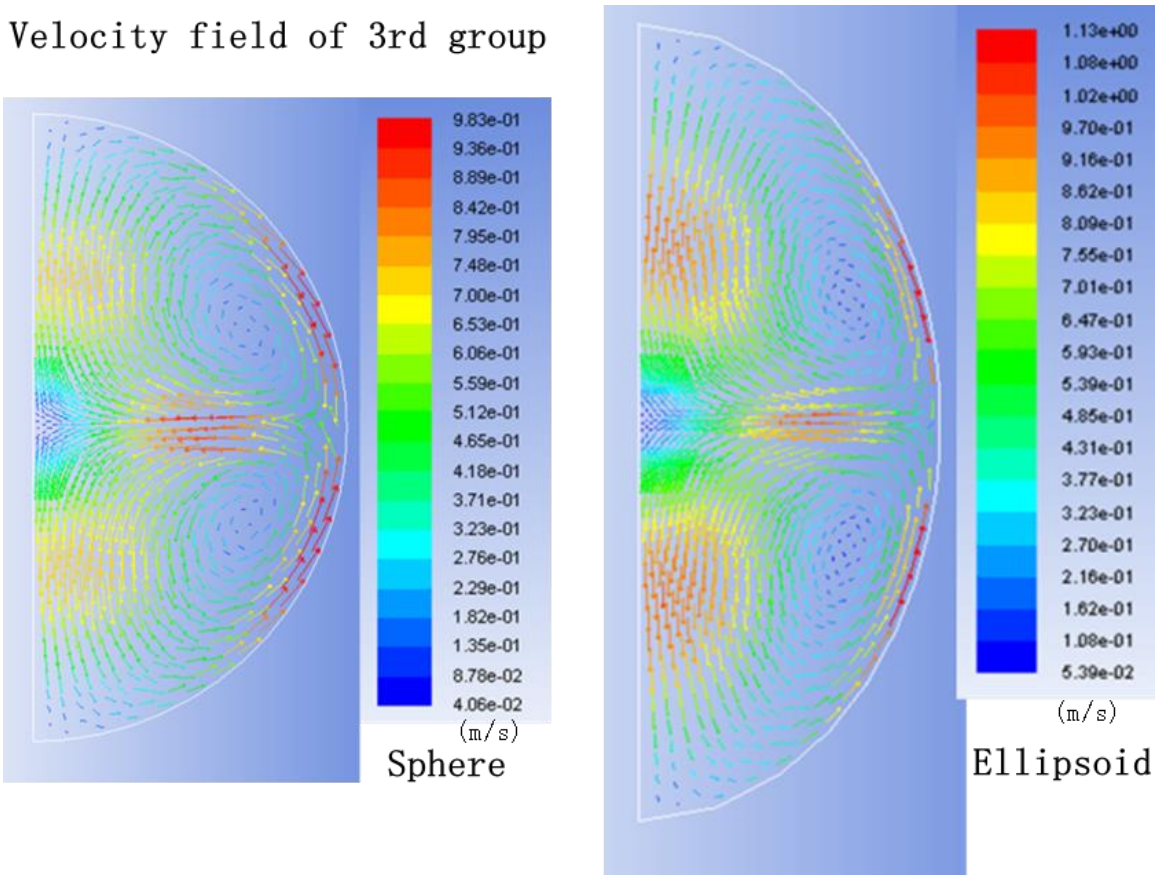

Figure 5.1: Left: Velocity field evaluated by sphere mesh (Re=11064.5); Right: Velocity field evaluated by ellipsoid domain (Re=11323.64).

The calculation of the steady state model eventually converged and figure 5.1 shows the simulation results of the velocity field with different meshes. (Figure 5.1, Left: the sample was regarded as a perfect sphere, Right: the shape captured from the experiment record). There are two symmetric loops in the pattern, which is very similar to the one obtained from laminar flow simulation. However, this result provides a time-averaged velocity value at each point, rather than

relaying the exact motion of the flow, and the arrow gives the direction of the time-averaged velocity. According to the legend corresponding to each mesh, the maximum value has reached up to around 1m/s. Thus, the Reynolds number can be calculated by equation (1.9) and turns out to be 11065 (Left) and 11324 (Right), which is too large to be considered laminar flow. ($Re \leq 600$ [1]) In the calculation, the reference length used by the sphere domain (Left) was the diameter of the droplet. While the short axis of the ellipsoid was regarded as the reference length of the deformed droplet for the shape of the deformed droplet was like between a sphere and a pipe.

Therefore, it is a turbulent flow. It can be concluded that under the experiment, conditions of the laminar-turbulent transition occurred; the internal convection became turbulent eventually.

Although derived from different meshes, the two patterns of velocity field are very similar, with two symmetric loops directed inward on the equator. The maximum values of velocity are also close, reaching up to 1m/s near the boundary of the sample surface. In fact, there is very little difference between two simulation results.

5.2 Transient model--Geometry

One hypothesis for the discrepancy of time to transition between the experiment and the steady-state model is that the flow becomes turbulent before reaching steady state. Accordingly, transient models adopting two kinds of geometries were constructed.

According to the experiment record, the Reynolds number should be around 800 and the maximum velocity of the fluid flow should be about 0.076m/s on at the onset of the laminar-turbulent transition. (Chapter 3)

From the video of the experiment, it took 0.371s for the fluid flow to become turbulent.

Two kinds of geometries have been tested in the 4th group of transient models. Compared with the time to transition from experiment—0.371s, there was no obvious difference of those obtained from two geometries which turned out to be 0.0025s and 0.0013s (Figure 5.2 and Figure 5.3). In other words, the internal fluid flow was accelerated to turbulence almost instantly, which is far different from the time to transition captured from the experiment, 0.371s. Therefore, the difference in the shape of the geometry cannot explain the discrepancy between the MHD models and the experiment result.

Since the velocity field obtained from transient model was not fully developed (Figure 5.4), the pattern of the velocity field was different from that of steady-state models (3rd group). The flow near the axis in the steady state model had a high velocity, while in the transient model, the convection near the axis show low velocity.

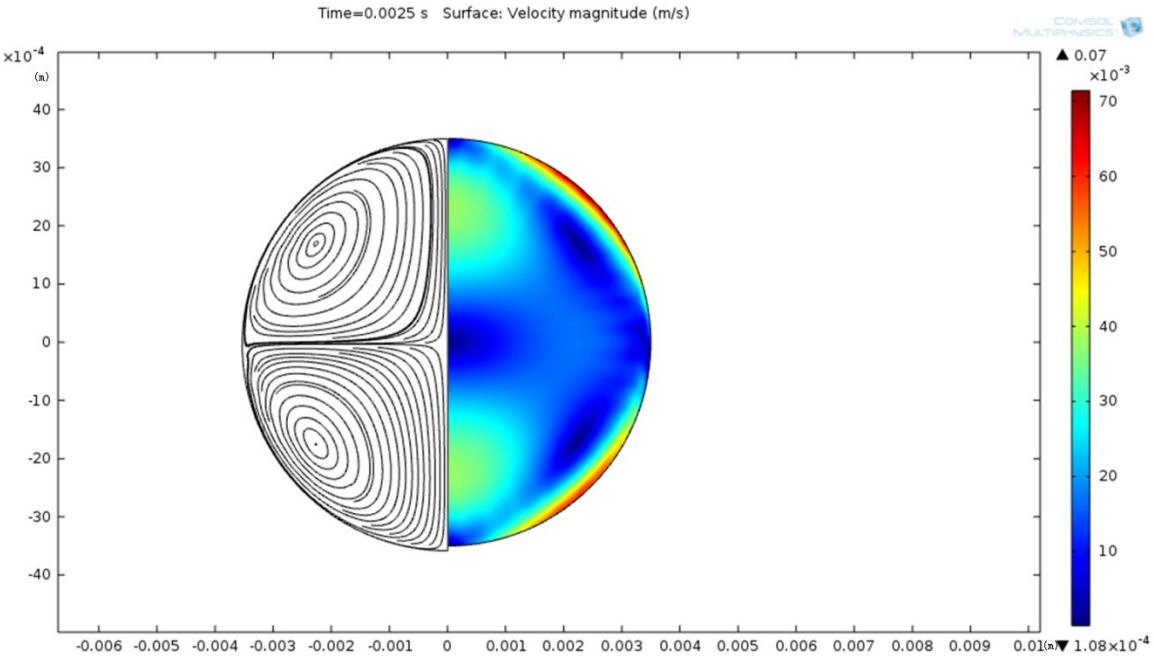

Figure 5.2: The velocity field and streamline obtained from the transient model with sphere geometry. The maximum velocity had reached up to 0.07m/s when the electromagnetic force was fully loaded. The Reynolds number was around 800.

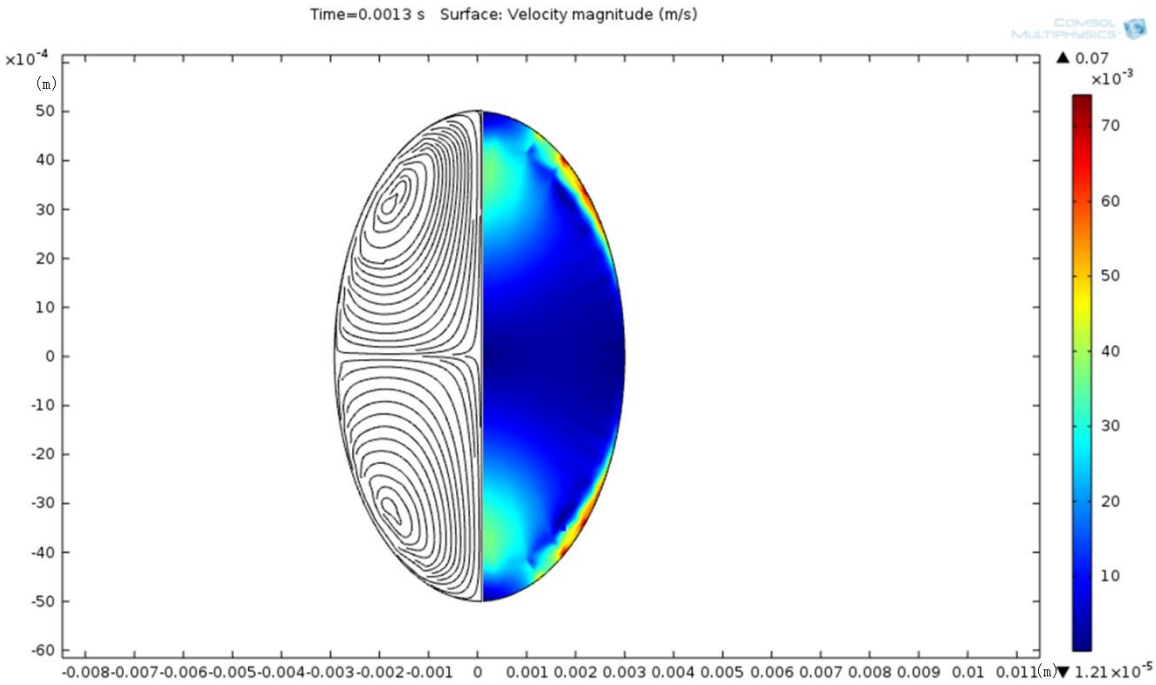

Figure 5.3: The velocity field and streamline obtained from the transient model with ellipsoid geometry. The Reynolds number had already reached up to about 800 at 0.0013s, which means the internal fluid flow was accelerated to turbulence immediately.

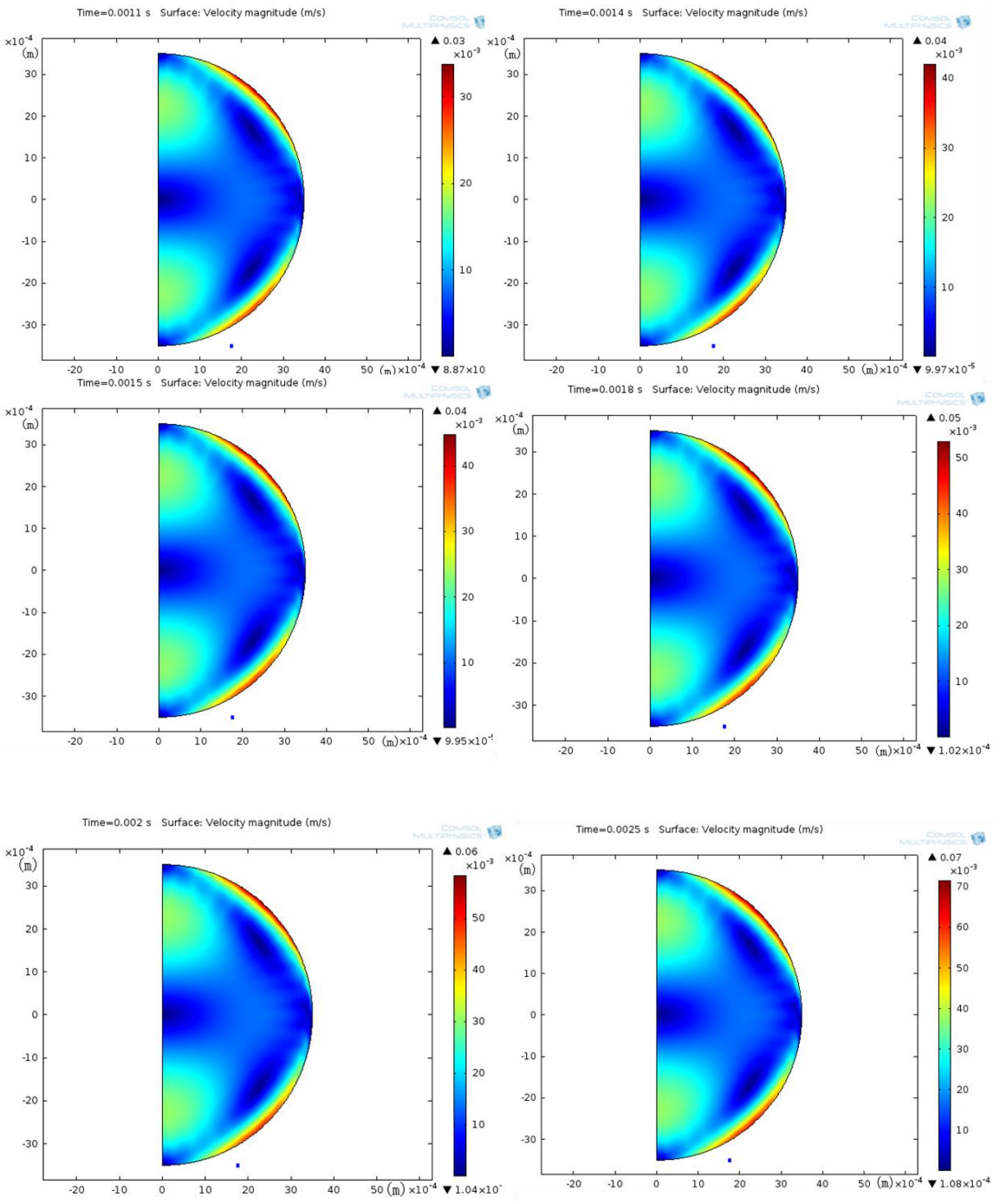

Figure 5.4: Frames before the maximum reached up to 0.07s, obtained from the simulation result of the velocity field.

The hypothesis that the internal fluid flow needed a longer time to become turbulent because of the less distributed force due to the deformed shape was denied. Although both geometries have

been tested, the fluid flow was accelerated sharply to become turbulence. The geometry did affect the time to transition (Sphere: 0.0025s; Ellipsoid: 0.0013s), but cannot explain the discrepancy between the experiment and the simulation.

5.3 Transient model—Boundary conditions

According to the experiment record, the solid tracer particles gathered around the equator to form a solid shell which was more like a wall than the free surface of droplet. Thus, the boundary conditions of the domain in the 5th group were composed of "slip" (liquid-free surface) and "non-slip" (solid) for liquid and solid surface. The area close to two poles of the sample were defined as "slip" for free surface while the band around the equator used "non-slip".

From the models adopting "slip+non-slip" boundary conditions, the figure 5.5 and 5.6 provide the velocity field and streamline when the Reynolds number reached up to around 800. Figures 5.7, 5.8, 5.9, 5.10 gave a view of how the "non-slip" boundary affects the fluid flow on the sample surface—the boundary layer developed (Figure 6.4 and Figure 6.6). The time to transitions calculated by the different geometries were 0.0026s and 0.003s respectively, which show little difference. Moreover, the time to transition did not last long enough to be comparable with the one captured from the experiment (0.371s). Thus the "slip+non-slip" boundary condition did affect the velocity field in the sample but was not the main factor to influence the time to transition.

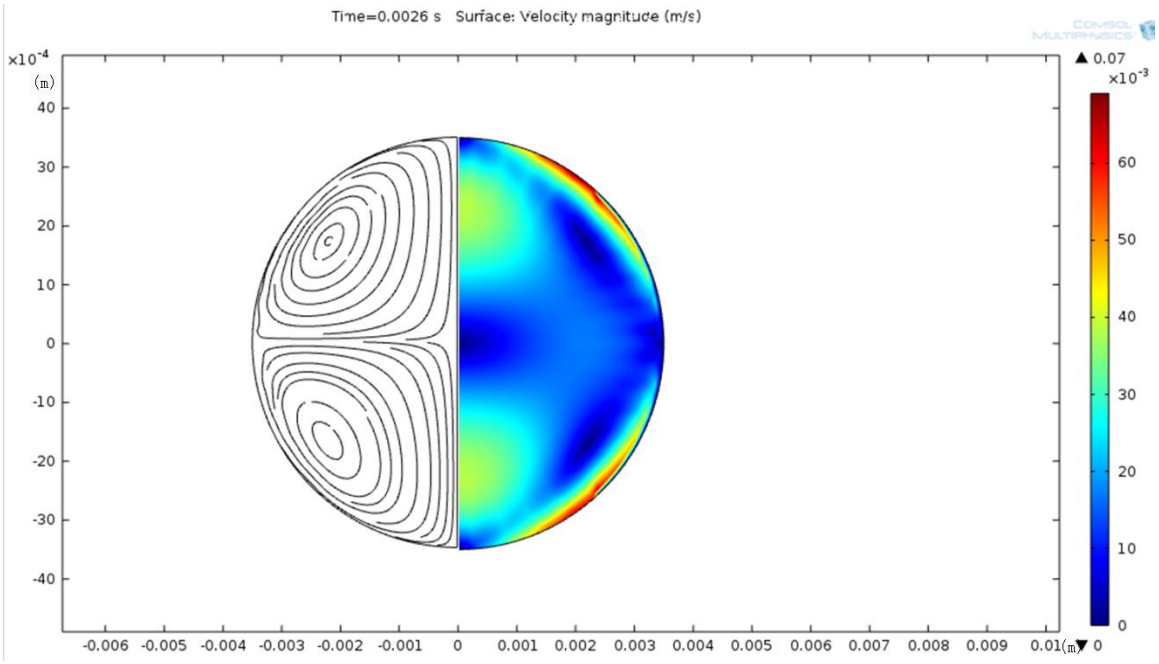

Figure 5.5: The velocity field and streamline obtained from the transient model with "slip+non-slip" boundary conditions and sphere geometry. The time to transition needed by the flow was very small, 0.0026s, which means the boundary conditions did not relate to the calculation result directly.

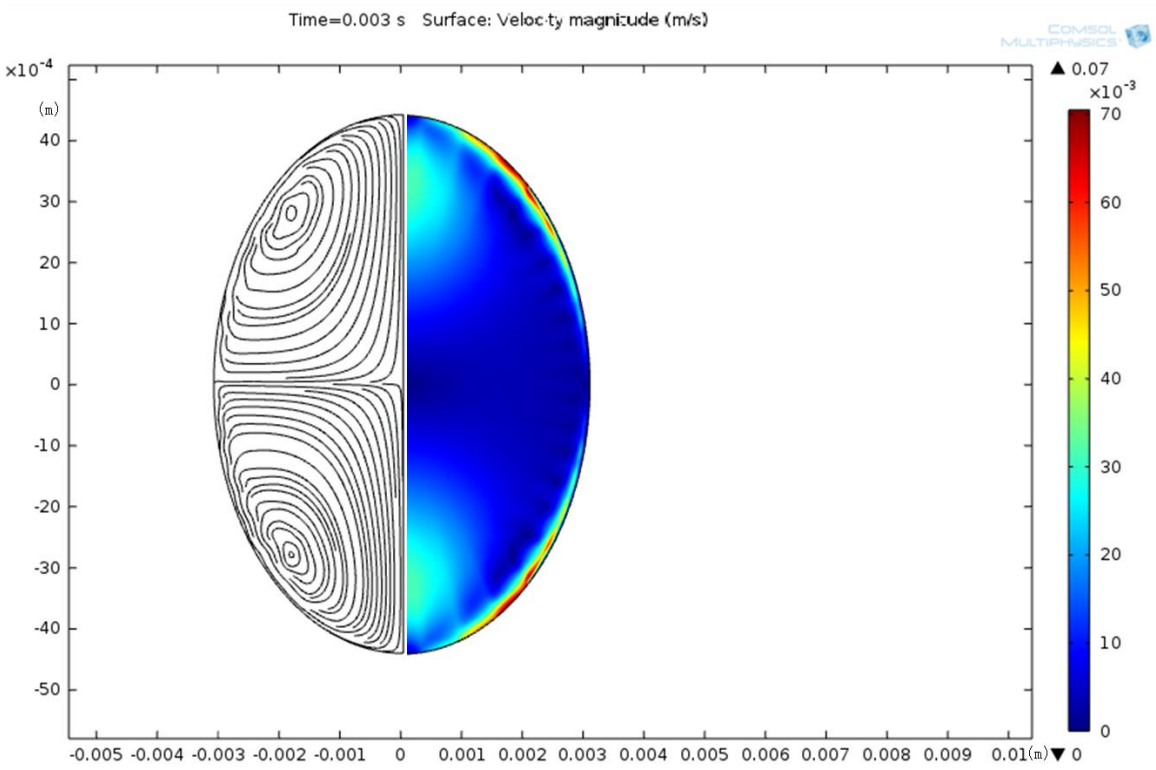

Figure 5.6: The velocity field and streamline obtained from the transient model with "slip+non-slip" boundary conditions and ellipsoid geometry. Time to transition required was still very short that only 0.003s, which means, the flow reached up to turbulence right after the electromagnetic force fully loaded.

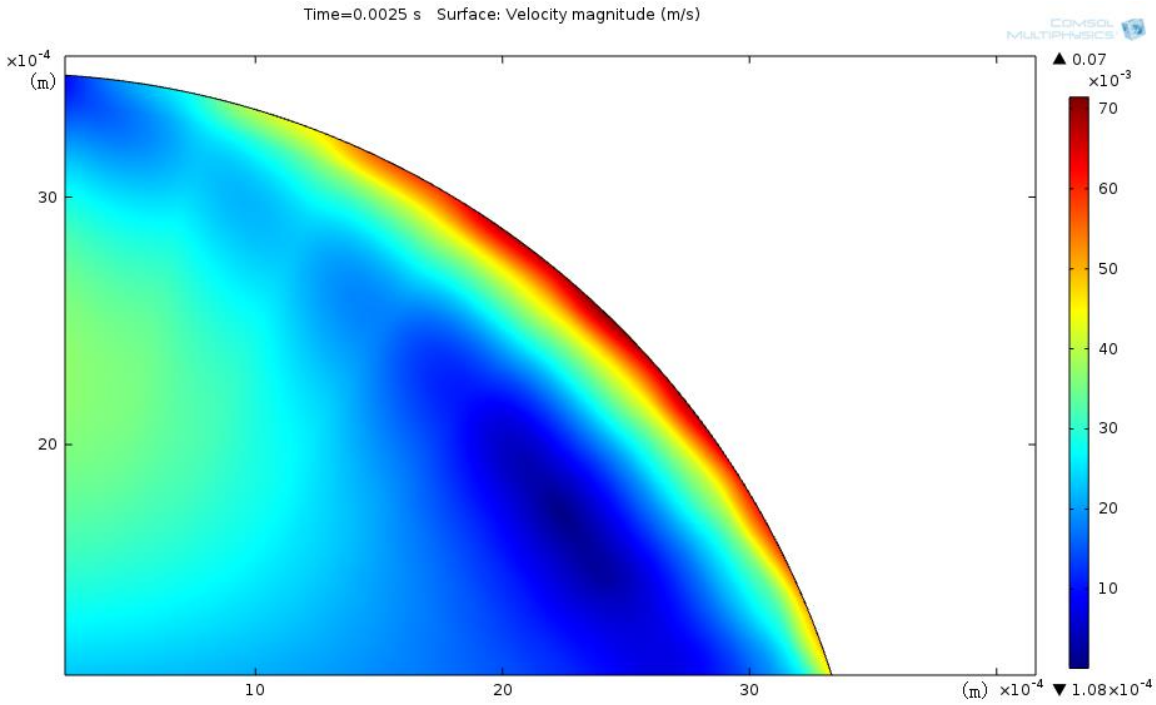

Figure 5.7: The velocity field near the sample surface in the 4th group of transient models with sphere geometry.

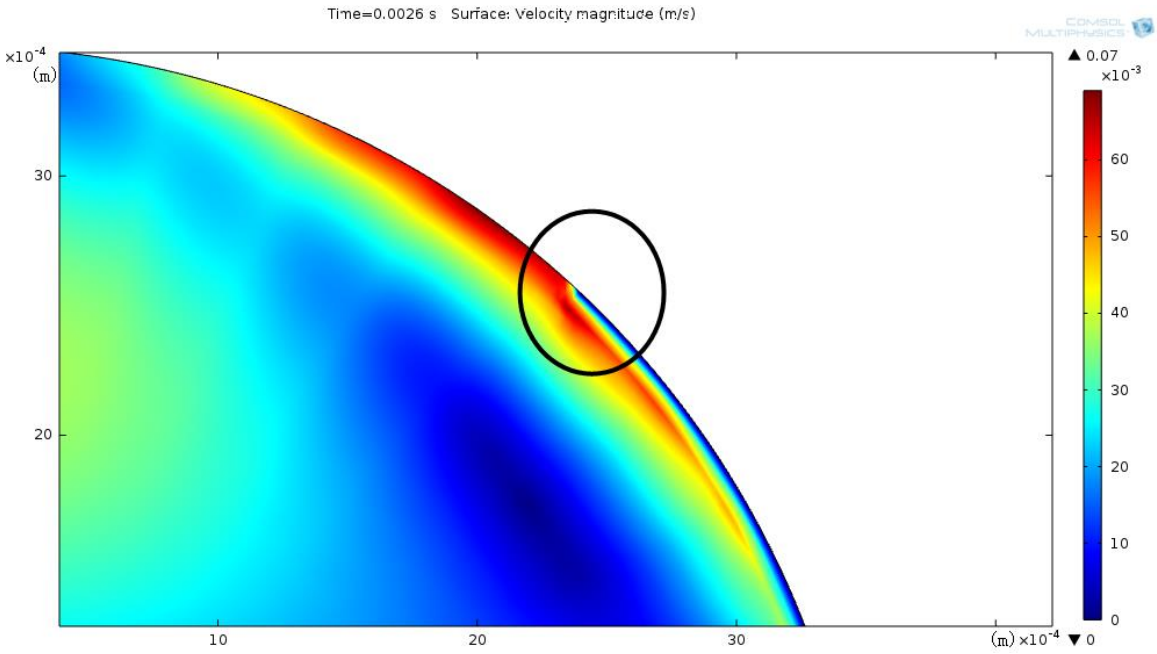

Figure 5.8: The velocity field near the sample surface in the 5th group of transient models with sphere geometry. The path of fluid flow near the surface was bended due to the "non-slip" boundary condition.

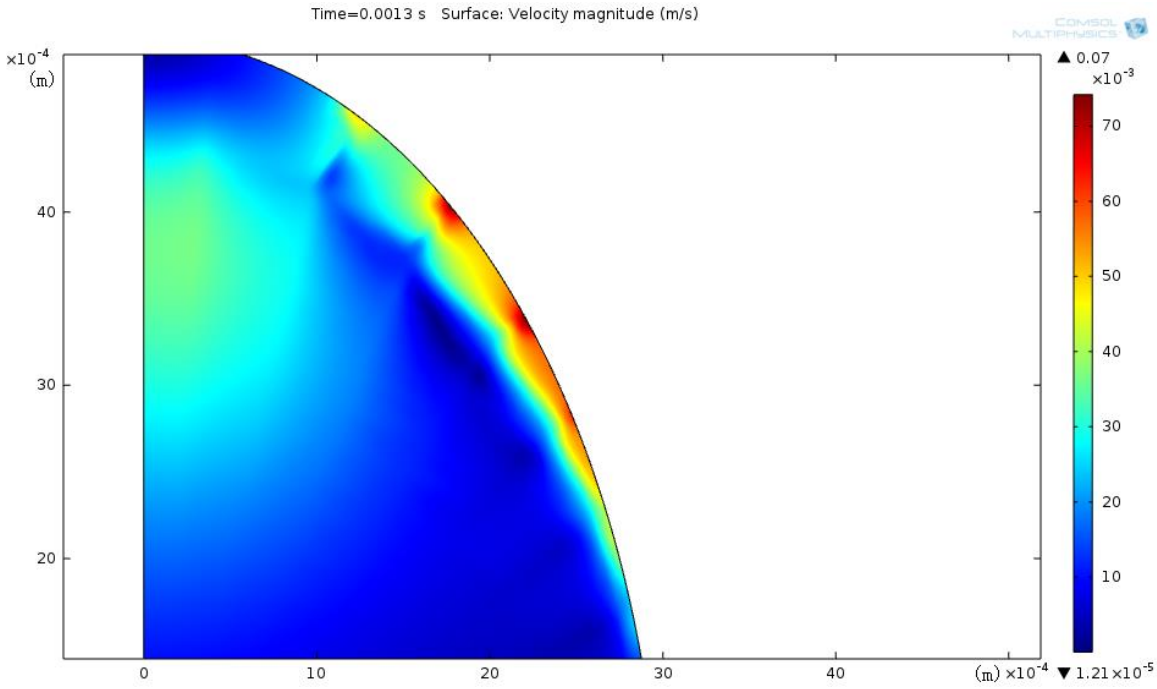

Figure 5.9: The velocity field near the sample surface in the 4th group of transient models with ellipsoid geometry.

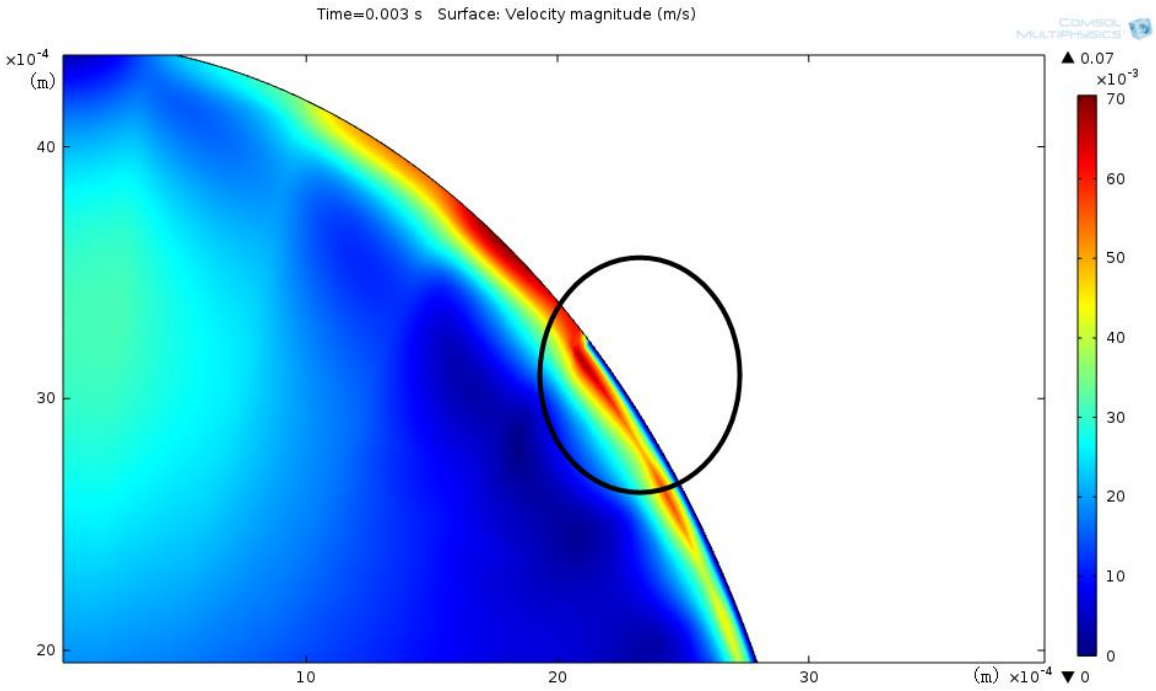

Figure 5.10: The velocity field near the sample surface in the 5th group of transient models with ellipsoid geometry. The path of fluid flow near the surface was bended due to the "non-slip" boundary condition too.

Therefore, the hypothesis that part of the solid band on the surface delayed the internal fluid flow was denied. The time to transition from the numerical models with "slip+non-slip" boundary conditions was too short to be compared with that from experiment, even using the ellipsoid geometry.

The following table shows the summery of the time to transition.

Table 5.1 Time to transition from the 5th and 6th group of models.

Time (s)	Sphere	Ellipsoid
"Slip" (5th group)	0.0025	0.0013
"Slip+Non-Slip" (6th group)	0.0026	0.003

It is obvious that the "slip+non-slip" boundary condition decreases the effect of geometry (Sphere vs Ellipse), but large effect on ellipse domain (Slip vs Non-slip).

5.4 Transient model—Solid core

The internal condition of the sample was taken into account too. The 3rd model showed that the convection should become turbulent eventually. However, the fluid flow required 0.37s to approach the laminar-turbulent transition according to the experiment record, while the model did this instantly. From the 4th and 5th groups of models evaluation, neither the shape of the geometries nor boundary conditions was the main cause of the delay of internal fluid flow. Thus, a model with an assumed solid core was tested. The figure 5.11 gave the calculation result.

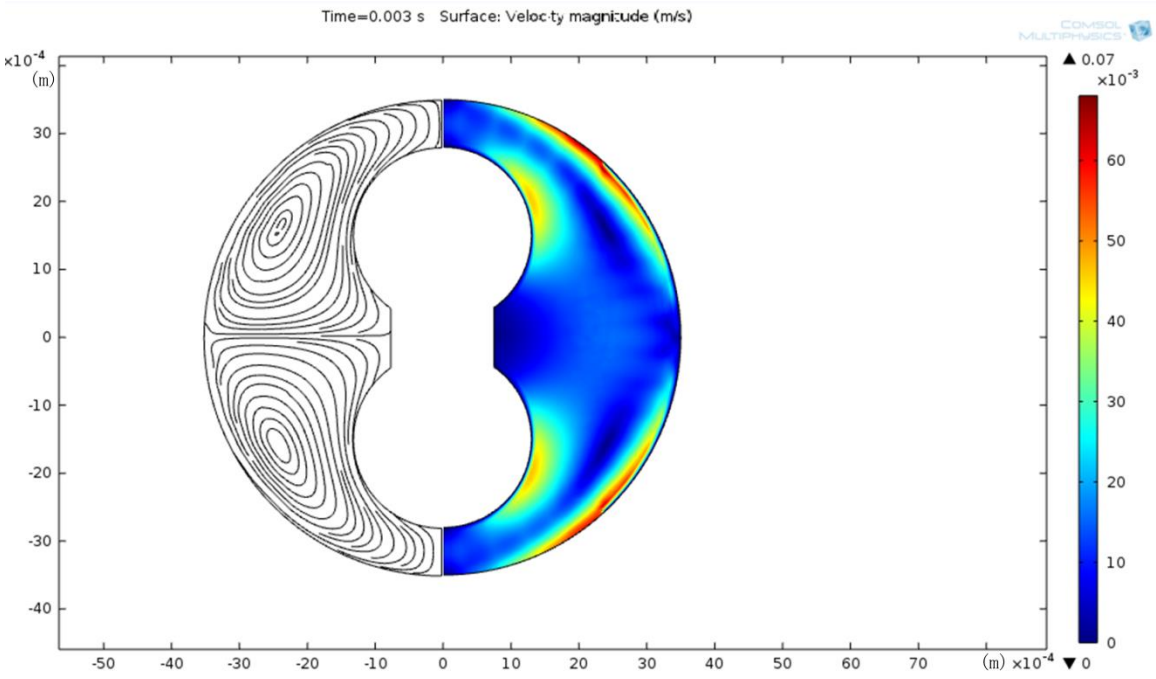

Figure 5.11: The velocity field and streamline obtained from the transient model with a solid core in shape of an apple core. There was little difference show in the time to transition, which is very short and was not comparable with the one from the experiment.

From the result, the fluid flow spent only 0.002s to reach up 0.07m/s, Reynolds number around 800, which was too short to explain the time to transition obtained from experience. According to the simulation result of 4th and 5th group, the flow was slow already where solid could be, so there was only little effect of solid inside. The assumption of solid core did not affect the numerical evaluation.

Moreover, since the experiment temperature 1472.15K (1199℃) on laminar-turbulent transition was higher than the melting point 1373.15K (1100℃), (see Phase Diagram Figure 4.1), there should be no large range of solid structures left in the core area to hinder the flow from being accelerated. The hypothesis of a solid part with a "tree-like" structure was cancelled out too, because if there were a "tree-like" structure filled in the liquid sample, the path of tracer particles would be bent instead of straight. From the experiment record, it was very clearly that the tracers were drawn from the pole and moving to accumulate the bright solid band directly.

Therefore, the hypothesis that there was still solid part left and the solid structure hindered the convection was disproven. Thus, the existence of internal solid structures does not explain the discrepancy.

CHAPTER 6

CONCLUSION

1. The tracer particles' movement on the sample surface provided the convection condition due to the small Stokes number. The top view of observation in the experiment gave a better insight of the internal convection, because the side view was obscured by a solid shell, probably of oxide.

2. The Reynolds number at the turbulent transition was estimated as approximately 860.

3. Although the flow observed from the video transitioned from laminar to turbulent, the Reynolds number calculated by steady state model was too large for the flow to be laminar at equilibrium. The flow might exist in a superlaminar state for a while before transitioning to turbulence. Moreover, the formation of eddies is a transient process that also takes some time. Therefore, the laminar-turbulent transition happened during the acceleration of the flow. The flow accelerated very fast, which is determined by the electromagnetic force and density of the flow on a given volume element.

4. Predicted time to transition showed a significant difference (~ up to 300 times) compared with the experiment.

5. The simulation results show that none of proposed hypotheses can explain the transition of the high velocity convection in this case of $NiAl_3$: the shape of the geometry, the boundary conditions, or a solid core. The simulations predict that the flow would become turbulent almost instantaneously after the droplet was fully molten. There are important physics shown by the simulation were not captured.

CHAPTER 7

FUTURE WORK

1. In the future work, new hypotheses need to be tested in simulations to explain the transient time of the high velocity in this case of $NiAl_3$.

2. New experiments should be designed which can be modeled more accurately. The internal convection should be quasistatic. To obtain slower transients, smaller forces or higher viscosity are required. In addition, a simpler boundary condition and geometry are good for the calculation too.

3. The experiments and numerical evaluation of the case from the literature [1] needs to be repeated to examine whether there were important physics not captured before.

BIBLIOGRAPHY

1. R.W. Hyers， G. Trapaga and B. Abedian: Laminar-Turbulent Transition in an Electromagnetically Levitated Droplet, Metallurgical and materials transactions B, 2003, Vol. 34B, pp. 29-36.

2. R.W. Hyers, D.M. Matson, K.F. Kelton, J.R. Rogers: Convection in Containerless Processing, Ann. N.Y. Acad Sci. 2004, 1027, pp. 474-94

3. G. Lohofer, J. Piller, American Institute of Aeronautics and Astronautics, 2001, AIAA 2002-0764

4. G. Lohoefer and J. Piller: The New ISS Electromagnetic Levitation Facility: MSL-EML, The Proceedings of the 40th AIAA Aerospace Sciences Meeting & Exhibit, Jan 14-17, 2002, Reno, NV.

5. R.W. Hyers: Ph.D. Thesis, Massachusetts Institute of Technology, Cambridge, MA, 1998

6. R.W. Hyers: Fluid flow effects in levitated droplets, Measurement science and Technology, 2005, Volume: 16 Issue: 2 pp: 394-401

7. J. Lee, D.M. Matson, S. Binder, M. Kolbe, D. Herlach, and R.W. Hyers: Magnetohydrodynamic Modeling and Experimental Validation of Convection Inside Electromagnetically Levitated Co-Cu Droplets, Metallurgical and Materials Transactions B, 2013

8. B.Q. Li: Effect of Convection on the Measurement of Thermophysical Properties Using Levitated Droplets, Annals of the New York Academy of Sciences. 2006,1077,pp1-32

9. M.P. Groover: Fundamentals of Modern Manufactureing, 2013, pp 239-245

10. A.B. Hanlon, R.W. Hyers, D.M. Matson: Modeling the effects of internal convection on dendritic evolution in stainless steel alloys, TMS, 2005

11. A.B. Hanlon, D.M. Matson, R.W. Hyers: Microgravity Experiments on the Effect of Internal Flow on Solidification of Fe-Cr-Ni Stainless Steel, Ann. N. Y. Acad. Sci., 2006, 1077, pp. 33-48.

12. A.B. Hanlon, D.M. Matson, R.W. Hyers: Internal convective effects on the lifetime of the metastable phase undercooled Fe-Cr-Ni alloys, Philisophical Magazine Letters, 2006, vol. 86, Issue 3, pp.165-174

13. I. Egry, G, Lohofer, I. Seyhan, S. Schneider, B. Feuerbacher: Viscosity and Surface tension measurements in microgravity, International Journal of Thermophysics, 1999, Volume 20, Issue 4, pp. 1005-1015

14. P.F. Paradis, T. Ishikawa, and S. Yoda: Non-Contact measurements of surface tension and viscosity of Niobium, Zirconium, and Titanium using an electrostatic levitation furnace, International Journal of Thermophysics, 2002, Volume 23, No. 3

15. R.K. Wunderlich, H-J. Fecht: Modulated electromagnetic induction calorimetry of reactive metallic liquids, Meas. Sci. Technol., 2005, Vol. 16, pp. 40

16. I. Egry: Thermophysical property measurements in microgravity, International Journal of Thermophysics, 2003, Volume 24, Issue 5, pp. 1313-1324

17. T. Iida and R.I.L. Guthrie: The physical properties of liquid metals, 1993, pp. 69-71

18. I. Egry, R. Brooks, D. Holland-Moritz, R. Novakovic, T. Matsushita, Y. Plevachiuk, E. Ricci, S. Seetharaman, V. Sklyarchuk, R. Wunderlich: Thermophysical properties of liquid Al-Ni alloys, High Temperatures-High Pressures, 2010, Vol. 38, pp. 343-351

19. D.M. Matson et al.: Contrasting electrostatic and electromagnetic levitation experimental results for transformation kinetics of steel alloys, Annals of the New York Academy of Sciences, 2004, pp. 435-46

20. J.M. Rogers et al.: Thermophysical property measurement and material research in the NASA/MSFC electrostatic levitator, AIP Conference proceedings, vol. 552 (Space Technology and Applications International Forum 2001), 2001, pp. 332-336

21. M.C. Flemings et al.: Levitation observation of dendritic evolution in steel ternary alloy rapid solidification (LODESTARS), NASA Science requirements document, 2003

22. D.J. Fair: Comparing electrostatic and electromagnetic levitation as a means for the study of phase transformations in steel alloys, M.S. Thesis, Department of Mechanical Engineering, Tufts University, 2004

23. R, Venkatesh, R.W. Hyers, D.M. Matson: The influence of internal and external convection in the transformation behavior of Fe-Cr-Ni alloys., TMS, 2004, Charolette, NC, U.S.

24. D.M. Matson: Growth competition during double recalescence in Fe-Cr-Ni Alloys, Materials in space—Science, Technology and Exploration, Vol. 551, pp. 227-234

25. R.B. Byrd, W.E. Stewart, E.N. Lightfoot: Transport Phenomena, 1960

26. H. Lamb: On the oscillations of a viscous liquid globe, Pro. Lond. Math. Soc. Vol. 13, pp. 51-66

27. S. Chandrasekhar: Hydrodynamic and Hydromagnetic Stability, 1961

28. H.F. Bauer, W. Eidel: Marangoni-convection in a spherical liquid system, Acta Astronautica, 1987, vol. 15, pp. 275-90

29. B.Q. Li, S.P. Song: Thermal and fluid flow aspects of electromagnetic and electrostatic levitation—a comparative modeling study, Microgravity Sci. Technol. pp. 134-43

30. J. Lee, J. Zhao, R. Wunderlich, and R.W. Hyers, The 5th ISPS, 2013, Orlando, FL

31. I. Egry, H. Giffard and S. Schneider: The oscillating drop technique revisited, Meas. Sci. Technol., 2005, Vol. 16, pp. 426-31

32. R.W. Hyers, G. Trapaga and M.C. Flemings: Surface tension and viscosity measurements in microgravity: results from Space Shuttle and parabolic flight experiments, 11th Experimental Methods for Microgravity Materials Science Symposium TMS (CDROM)

33. H-J. Fecht and R.K. Wunderlich: The thermolab project: thermophysical properties of industrially relevant liquid metal alloys, First International Symposium on Microgravity Research and Applications in Physical Sciences and Biotechnology, 2001, Vol. 1 and 2, pp. 545-52

34. R. W. Hyers and G. Trapaga: Measurement of the viscosity and surface tension of undercooled liquid metals under microgravity conditions, Solidification ed S.P. Marsh, N. B. Singh, P. W. Voorhees and W.H. Hofmeister (Warrendale, PA: TMS) pp. 23-32

35. I. Egry, G. Lohofer, I. Seyhan, S. Schneider and B. Feuerbacher: Viscosity of eutectic $Pd_{78}Cu_6Si1_6$ measured by the oscillating drop technique in microgravity, Appl. Phys. Lett., Vol. 73, pp. 462-3